

AD-A139 719

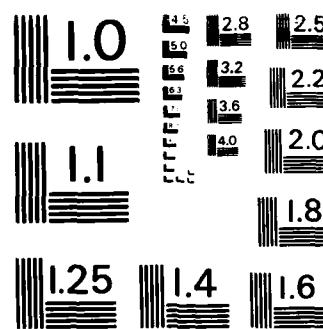
ELECTRIC VEHICLE MODELING AND SIMULATION(U) AIR FORCE
INST OF TECH WRIGHT-PATTERSON AFB OH SCHOOL OF
ENGINEERING A R DEWISPELARE AUG 83 AU-AFIT-EN-TR-83-4

1/1

UNCLASSIFIED

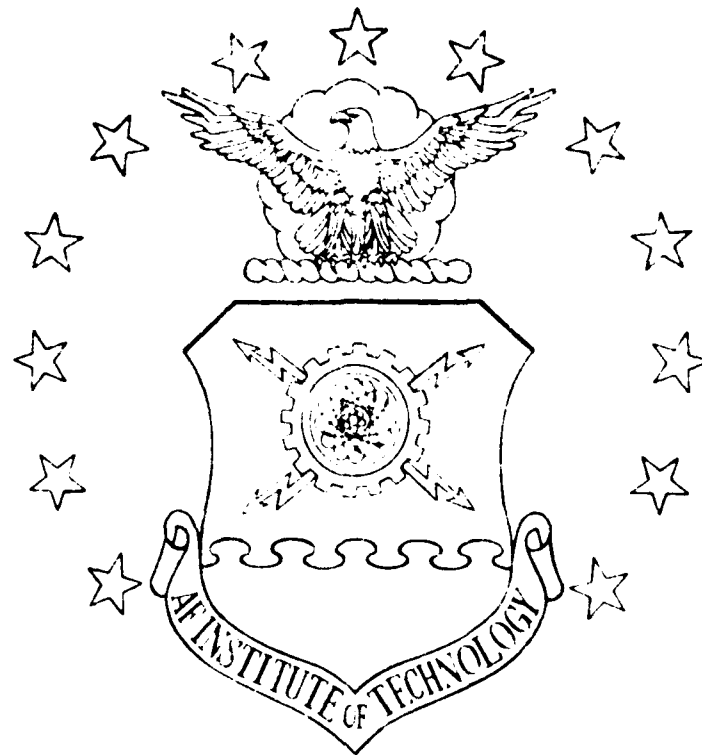
F/G 13/6

NL



MICROCOPY RESOLUTION TEST CHART
NATIONAL BUREAU OF STANDARDS - 1963 - A

AD A139719



ELECTRIC VEHICLE MODELING
AND SIMULATION

TECHNICAL REPORT

AU-AFIT-EN-TR-83-4

Aaron R. DeWispela

This document has been approved
for public release and sale. Its
distribution is unlimited.

DEPARTMENT OF THE AIR FORCE
AIR UNIVERSITY (ATC)

AIR FORCE INSTITUTE OF TECHNOLOGY

DTIC FILE COPY

DTIC
ELECTED
MAR 29 1984

A

Wright-Patterson Air Force Base, Ohio

84 03 20 00

(Handwritten mark)

ELECTRIC VEHICLE MODELING
AND SIMULATION

TECHNICAL REPORT

AU-AFIT-EN-TR-83-4 Aaron R. DeWispelare

SERIALIZED
ELECTRO.
MAR 23 1984

A

This document contains neither recommendations nor conclusions of the Defense Department. It has been approved for public release and may be distributed freely.

ELECTRIC VEHICLE MODELING
AND SIMULATION

AARON R. DEWISPELARE
Associate Professor of Systems and
Aerospace Engineering

Technical Report AU-AFIT-EN-TR-83-4
August 1983

Approved for Public Release
Distribution Unlimited

School of Engineering
Air Force Institute of Technology
Wright-Patterson Air Force Base, Ohio

Table of Contents

Abstract	ii
List of Symbols.	iii
I. Introduction	1
II. Modeling	4
III. Simulation Methodology	23
IV. Hardware Implementation of the EV.	35
V. Additional Concept Investigation	41
VI. Summary and Conclusions.	56
Bibliography	57
Appendix - EVSIM Program Listing	60



Accession For	
DIS	SR&I
DIS	TAR
DIS	Unpublished
DIS	Classification
Distribution/	
Availability Codes	
Dist	Avail and/or Special
A	
A	
A	

Abstract

The forecasting of the performance of electric vehicles has revealed many discrepancies when compared to actual test data. An electric vehicle computer simulation program was developed to ameliorate this deficiency. The approach was to establish a very comprehensive and flexible vehicle model and simulate its operation on a realistic driving cycle. The driving cycle selected was the Federal Urban Driving Sequence. A thorough vehicle model was established that incorporates aerodynamic drag, rolling resistance, both rotational and translational inertial effects, and component by component dynamic power train efficiencies. Battery discharge performance is tracked by a fractional-utilization algorithm with corrections for short-term discharge effects. The simulation compares required power obtained from the driving cycle speed schedule and vehicle model characteristics with the available power at the motor for each time increment of the driving cycle to compute battery fraction used and deviation from the speed schedule when available power is insufficient. These results of the simulation can be used to evaluate an existing vehicle's performance or, if desired, to develop vehicle parameters to obtain a specified performance level. An application of the program to develop a suburban passenger vehicle is included to demonstrate the simulation's utility. A test bed vehicle was constructed and tested to verify the simulation. Additional aspects such as microprocessor based controllers including implementation of an optimal control law were investigated to gain insite into the efficiency and performance trade-offs of such a system.

List of Symbols

A	=	Frontal area (m^2)
AR	=	Axle ratio
BM	=	Battery mass (kg)
c	=	Battery capacity (amp \cdot hr)
C	=	Coefficient of resistance
CM	=	Chassis mass (kg)
d	=	Disturbance
DF	=	Discharge fraction
E	=	Electromagnetic force (volts)
F	=	Force (nt)
FA	=	Frontal area
FM	=	Fixed mass (kg)
g	=	Acceleration of gravity (m/sec^2)
GR	=	Gear ratio
GMV	=	Gross vehicle mass (kg)
I	=	Current (amps)
J	=	Polar moment of inertia (kg \cdot m^2)
k	=	Motor torque constant (weber \cdot rpm) $^{-1}$
k*	=	Motor proportionality constant (ohms/rpm)
L	=	Inductance (henrys)
M	=	Torsional moment (nt \cdot m)
MCF	=	Mass correction factor
MM	=	Motor mass (plus hybrid components if applicable) (kg)
n	=	Shaft speed (rpm)
P	=	Power (watts)
PM	=	Payload mass (kg)

PP = Rated power fraction (%)
PSPD = Rated speed fraction (%)
Q = Setpoint state weighting matrix
r = Rolling radius (m)
r = Control weighting scalar
R = Resistance (ohms)
t = Time (sec)
T = Temperature (C)
v = Speed (m/sec)
V = Potential (volts)
 v_a = Vehicle velocity
 v_c = Controller voltage
 v_m = Motor voltage
 V_M = Vehicle mass (for test conditions) (kg)
W = Energy (watt · sec)
n = Efficiency (%)
ρ = Density (kg/m^3)
φ = Field strength (webers)
 ω = Angular velocity (sec^{-1})

Additional Subscripts

a = Armature	IN = Input
A = Axle	M = Motor
AC = Acceleration	MAX = Maximum
B = Battery	OUT = Output
c = Cell	r = Rated value
C = Controller	R = Rolling drag

D = Air drag

T = Transmission

f = field

H = Hybrid

ELECTRIC VEHICLE MODELING AND SIMULATION

I. Introduction

This report describes recent efforts of the Air Force Institute of Technology in the area of Electric Vehicle (EV) research aimed at developing models to aid government agencies in petroleum fuel conservation for ground transportation. Interest in petroleum fuel conversation and alternative fuel usage has greatly increased in the past decade. The USAF and other government agencies are becoming especially interested in reducing foreign oil dependence. While NASA and USAF-sponsored projects have achieved significant technological advances toward reducing aircraft fuel usage, only recently has complimentary interest been shown toward economic alternatives to the gas-powered ground vehicle.

Background

In the mid-1970's, replacement of various small conventional vehicles with electric-driven equivalents became an item of interest with Air Force Logistics Command (AFLC/USAF). The maintenance engineering branch of AFLC conducted several projects aimed at reducing operating costs of light intra-base utility vehicles by substitution of standard size vehicles with low-powered gasoline or electric vehicles (Ref 33). General conclusions were favorable toward the small electric vehicles even though their operating costs per mile during one 14-month test period were actually somewhat higher than the gas-powered alternatives (Ref 6). Further evidence of USAF electric vehicle interest came in May 1978, when an Air Command and Staff College research study investigated the practical and economical feasibility of using these vehicles for several on-base missions (Ref 34). This study concluded that electric vehicle operating costs were nearly equal to standard vehicles, but that the higher initial investment and limited performance of electric vehicles, due partly to their rudimentary state-of-the-art development, made them undesirable at that time. (Note that the operating expenses for the above study were based on energy costs of 4¢ per kilowatt hour of electricity and 40¢ per gallon of gasoline). A further recommendation of the report, however, was that the USAF become actively involved in the electric vehicle tests sponsored by the Department of Energy (DOE).

This DOE program was established by Public Law 94-413, "Electric and Hybrid Vehicle Research, Development, and Demonstration Act of 1976." Among other things, it authorized the Energy Research and Development Agency (ERDA, now absorbed into DOE) to test 7,500 electric and hybrid vehicles within five years. Public Law 95-238, signed in February 1978, amended this Act, including an extension of the demonstration phase through 1986. In July 1980, by DOE interagency Agreement DE-AIOI-80CS50208 (Ref 8), the USAF became formally involved with the demonstration program. This agreement committed the USAF to procure and test 15 electric vehicles to be distributed to three different locations for a total period of four years.

An early product of Public Law 94-413 tasking was a very thorough NASA report titled, "State-of-the-Art Assessment of Electric and Hybrid Vehicles" published in September 1977. The purpose of this report was to characterize the current state of electric and hybrid vehicle development through controlled tests of commercially available and experimental vehicles, through manufacturer-supplied data, and through user reports. Data was thus obtained from nearly 200 different electric and hybrid vehicles. Of particular significance, the report discovered extreme variances between similar vehicles in their overall energy efficiency (.015 to .8 kwh/km/1000 kg) and in their user-experienced performance versus manufacturers' claims or controlled laboratory test results.

Objectives

In lieu of the increased interest among government agencies (including very recently the USAF) as well as the observed lack of sophistication among many electric vehicle designs, the prime objective of this effort was to provide an accurate method to simulate electric vehicle systems. The goal was to provide a computer simulation useful both for new system design as well as evaluation of existing competitive designs. To offer these capabilities, the model had to be flexible enough to accommodate a wide variety of design options.

Preliminary results of the simulation were used to select a viable electric vehicle system to compete economically with conventional USAF passenger cars. This system was then incorporated into a low-cost vehicle which was designed and built for data-gathering and simulation validation as well as a flexible test-bed to investigate other EV options such as controller performance.

Approach

Based upon the lack of correlation between actual performance and early simulation prediction attempts (Ref 32), an early priority of this effort was to carefully select an operating sequence to most realistically portray on-the-road vehicle use. Once determined, road load power requirements could be easily calculated. The dynamic efficiency of each power train component was then individually modeled and assembled together into an interrelated complex vehicle model. Net power requirements to the motor and/or engine could then be obtained. A multi-variable battery model was combined with controller characteristics to determine available power to the motor under any condition. A comparison between this available power and the required power was used to predict the sufficiency of the power supply and/or the performance deviation from the prescribed driving cycle (speed schedule). Further features of the battery model enabled the simulation to track net energy usage and the extent of nominal discharge. Final outputs of the simulation were then the average energy cost per kilometer as well as the amount of battery consumed per cycle, which together with estimated procurement and maintenance costs, can be used as a measure of merit for a selected system.

The basic approach toward achieving the objective of test vehicle design and construction was to use an existing chassis combined

with readily-available electric power components. This approach, while not providing a completely system-optimized vehicle, allowed quick construction of a low-cost test-bed for further component optimization investigation.

Performance Requirements

The flexibility of the vehicle model and simulation developed later in this study allows their use for a variety of vehicle types and missions. However, the prime vehicle envisioned throughout the study and which formed the basis for the test vehicle was a compact four-passenger sedan. This type of general purpose vehicle is used by the USAF for both on- and off-base missions. Table I lists the performance goals that were established for this type of vehicle based on the expressed desires of USAF vehicle managers (Ref 34) and analysis of some reasonable off-base mission requirements. A vehicle designed to minimally meet the Table I performance would be primarily an urban or on-base vehicle, but would be capable of certain high speed, extended range trips. The 90 km/hr top speed with 80 km/hr cruise allows limited use of the vehicle on typical suburban routes, while the 0 to 50 km/hr acceleration satisfies typical urban driving demands (Ref 32).

TABLE I

Baseline Performance

Payload	4 Passenger (270 kg)
Top Speed	90 km/hr
Acceleration 0 to 50 km/hr	15 sec
Range	
Urban	80 km
80 km/hr cruise	60 km

For a test vehicle with an estimated gross mass of 1200 kg and frontal area of 1.9 m², published data (Refs 17, 23) indicated that the 90 km/hr speed translated to approximately 12 kw of required motor power, whereas the 0 to 50 acceleration required approximately 22 kw. The apparent critical parameter in electric vehicles, however, is total energy storage capacity rather than maximum power available (Ref 15). Multiplying the two-hour high speed cruise requirement by an estimated 10.5 kw power requirements for 80 km/hr resulted in a net required energy storage of 21 kwh. These power and energy requisites based on the Table I performance then became important criteria for selection of the electric drive system for the test vehicle.

With the vehicle performance requirements defined, the modeling of appropriate classes of subsystems could now proceed.

II. Modeling

The basis for any simulation is established by the models it incorporates. The EV simulation is composed of models of vehicle retarding forces, vehicle body and subsystems such as drive train, controller, batteries and hybrid engine.

Derivation of Road Loads

For travel on level roads, the combined vehicle retarding forces can be divided into the rolling resistance, air resistance, and acceleration forces. Road grade and wind were not explicitly modeled in this effort because standard driving cycle tests do not include them. In Chapter V, both grades and wind gusts were included as disturbances when investigating controller robustness.

Rolling Resistance. The force required to move any vehicle at constant speed without considering aerodynamic or powertrain drag is developed from the work performed in flexing the tire casing, the work in compressing the road surface under the tire, and the frictional work from tire slip. As such, this retardant force is logically a function of tire design, inflation pressure, vehicle weight, rolling surface, and vehicle speed. The dimensionless parameter that combines these variables is the coefficient of rolling resistance C_R . The rolling resistance F_R is then simply:

$$F_R = C_R \cdot VM \cdot g \quad (1)$$

where VM is the vehicle test mass. Data shown on Fig 1 represents the C_R of radial ply tires rolling on a hard, smooth surface (Ref 32). This information was used to obtain the following continuous equation for C_R versus speed v :

$$C_R = C'_R + (2.09 \cdot 10^{-7})v^{2.8} \quad (2)$$

C'_R represents the limiting value of C_R at zero speed (in the case of Fig 1, C'_R would equal .0105). The speed v in Eq (2) is expressed in m/sec. Combining Eqs (1) and (2) then results in the final equation for rolling resistance:

$$F_R = \{C'_R + (2.09 \cdot 10^{-7})v^{2.8}\}VM \cdot g \quad (3)$$

which results in newtons force with VM expressed in kilograms. Strictly speaking, Eq (3) is correct only for straight-ahead driving; during any turn the tires must also generate a side force through a slip angle. This side force then combines vectorially with F_R to produce the net resistance. However, most urban turns require slip angles of less than five degrees which produces a negligible increase in resistance. While C'_R is left variable to accommodate different tire types, it also can be modified to include grade resistance. Since grade resistance is simply the downhill component of the vehicle weight, i.e. the sine of the slope times the vehicle weight, the sine of the slope may be added to C'_R to arrive at the combined rolling resistance.

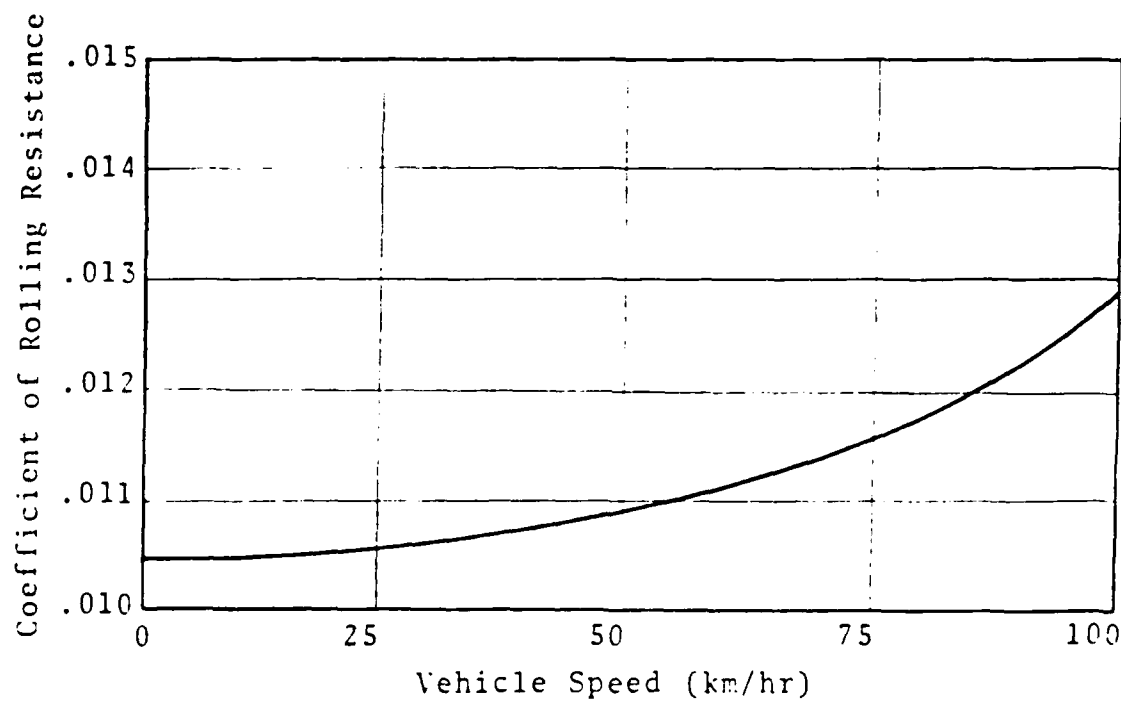


Fig 1. Rolling Coefficient for
Radial-Ply Tires

Aerodynamic Drag. At constant speeds above 60 km/hr, air resistance becomes the dominant retarding force for most vehicles (Ref 28). This source of drag comes from both viscous skin friction as well as form or pressure drag. The form drag caused by the low pressure zone behind the vehicle is dominant factor contributing approximately 90 percent of the total airdrag (Ref 42). In linearized form, the total air resistance force F_D is given by:

$$F_D = \left(\frac{\rho}{2}\right) v^2 \cdot A \cdot C_D \quad (4)$$

where ρ is the ambient air density, A is the projected vehicle area in the direction of motion, and C_D is a dimensionless parameter accounting for the shape of the vehicle. The air density ρ is, of course, a function of ambient pressure and temperature. However, normal atmospheric pressure variance causes only minimal density changes. Therefore, replacing ρ in Eq (4) with its value at standard pressure, while maintaining its temperature dependence, results in:

$$F_D = \left(\frac{176.4}{273^{\circ} + T}\right) v^2 \cdot A \cdot C_D \quad (5)$$

which provides newtons force with temperature T in Celsius.

Acceleration Forces. In realistic urban driving cycles, the inertial resistance to acceleration will, at times, be much larger than either the rolling or air resistance. Besides the translational effects on the vehicle mass:

$$F_{AC} = VM\left(\frac{dv}{dt}\right) \quad (6)$$

the angular accelerations applied to the rotating masses also produce significant inertial reactions. The acceleration torque M_{AC} due to rotary inertia is:

$$M_{AC} = \Sigma J \frac{d\omega}{dt} \quad (7)$$

where J is the moment of inertia for each rotating mass and $\frac{d\omega}{dt}$ is the respective angular acceleration. Chapter IV goes into more depth on the modeling of this rotary inertia term and how its effect is combined with Eq (6).

Calculation of Road Load Power. For use in the simulation, the calculated resistive forces (Eqs 3, 5, and 6) need to be converted into a required power as a function of time. An incremental approach was used which, for simplicity, assumes constant acceleration for each one-second time interval. The average speed can then be used in Eqs (3) and (5) while the acceleration term in Eq (6) becomes simply the incremental speed difference divided by the one-second time interval. Thus, the combined road forces for any increment are reduced to an average force over that increment. Required power can then be obtained by multiplying this combined force times the average velocity. This mid-interval power is not assumed constant throughout the increment, thus the input energy W is calculated by:

$$W = \int P \cdot t \quad (8)$$

where the integration of power P is taken over each time increment. Substituting $P = F \cdot v$ where F is the combined resistive forces and $v = t(\frac{\Delta v}{\Delta t}) + v_o$ into Eq (10) yields:

$$W = \int F(t) \frac{\Delta v}{\Delta t} + v_o dt \quad (9)$$

F is assumed constant for any time increment, thus integrating

$$W = F \left\{ \left(\frac{v_1 - v_o}{2\Delta t} \right) \Delta t^2 + v_o \Delta t \right\} \quad (10)$$

or

$$W = F \left\{ \frac{v_1 + v_o}{2} \right\} t = F \cdot \bar{v} \cdot \Delta t \quad (11)$$

and recognizing the $P = F \cdot \bar{v}$, where \bar{v} is the average speed for any increment, results finally in

$$W = P \cdot \Delta t \quad (12)$$

This work W then represents the incremental energy required at the rear wheels to meet the road load demands. Modeling of the vehicle resistance parameters and power train losses is now required to determine the necessary battery output to overcome this road load.

Vehicle Mass and Frontal Area

The vehicle mass and frontal area are the primary parameters used in determining road loads. As shown in Eqs (3) and (6), the vehicle mass effects both the rolling resistance and the acceleration loads. The gross vehicle mass may be considered to be represented by

$$VM = CM + FM + PM + BM + MM \quad (13)$$

where

GVM = gross vehicle mass
CM = chassis mass
FM = fixed mass
PM = payload mass
BM = battery mass
MM = motor mass (to include controls and hybrid engine mass if applicable)

The chassis mass includes all the basic structural materials in the vehicle which are designed to support the entire gross vehicle weight. Items such as the frame, suspension, wheels, and tires are included in this category. This mass is, therefore, a function of the gross vehicle mass and for passenger vehicles is typically (Ref 2) related as

$$CM = .23(GVM) \quad (14)$$

However, in this model, the chassis mass includes an adjustment for a fixed-ratio transmission and, hence, was set to

$$CM = .26(GVM) \quad (15)$$

The fixed mass figure represents all non-structural vehicle components which are related to the selected vehicle type and payload rather than directly to the power system or gross vehicle mass. Passenger seats, instruments, body panels and accessories are included in this category.

While maximum payload mass must be used in determining the gross vehicle mass and, hence, the chassis mass, the performance predicted through this simulation is based on a more normal one-half maximum payload. Combining this factor with Eq (13) results in a vehicle test mass VM as

$$VM = GVM - PM/2 \quad (16)$$

where, from Eqs (13) and (15)

$$GVM = .26(GVM) + FM + PM + BM + MM \quad (17)$$

or finally

$$VM = (FM + BM + MM)/.74 + .85(PM) \quad (18)$$

While the above test mass satisfies the requirements for obtaining rolling resistance, and additional factor of effective rotary mass must be taken into account to predict acceleration loads. Rotating mechanisms can conveniently be divided into two categories: those which rotate at speeds fixed to the vehicle speed (such as tires, wheels, and axles) and those which rotate at the engine or motor speed (such as clutch, flywheel, and crankshaft or armature). While it is possible to analytically obtain values for both categories by summing individual component angular momenta (Ref 26), the most reliable results are obtained experimentally. The net effect of both categories can be resolved into an equivalent mass located at the rim of the wheels. Since this equivalent mass is now traveling at the vehicle speed, it can be considered to undergo the same acceleration as the rest of the vehicle mass does. The rotating power train component mass is proportional to the vehicle mass and can, therefore, be considered to be a multiplicative mass correction factor. This factor relates shaft speed to wheel rim speed via the rolling radius and overall gear reduction ratio. Experimentally derived data (Ref 28) for four-wheel passenger vehicles suggests an equivalent inertia effect of about two percent of the vehicle's mass for the first category of wheel-rotation speed components. The second category can be shown to contribute an equivalent mass, varying quadratically with the shaft speed/vehicle speed ratio. The equivalent vehicle mass then to be considered during any acceleration period is the product of the vehicle test mass VM and the mass correction factor MCF where

$$MCF = 1.02 + .000294\left(\frac{AR \cdot GR}{r}\right)^2 \quad (19)$$

where AR and GR are axle ratio and transmission ratio respectively, and r is the tire rolling radius in meters. While the data (Ref 28) to derive Eq (19) above was obtained from conventional gas-engined vehicles, the largest contributor to the second half of this equation is the clutch-flywheel assembly which is generally left intact for multi-ratio electric vehicles.

The frontal area of any optimally-designed vehicle will also, in general, be a function of the vehicle mass. While geometric up-scaling of any volume (i.e. mass) suggests a corresponding two-thirds power increase in any exposed areas, in actuality, more massive vehicles tend toward a higher proportion of non-payload to payload volume and are, therefore generally denser. This tendency, coupled with practical passenger space/vehicle width considerations which result in larger fineness ratios with more massive vehicles, causes actual frontal area ratios to vary at a somewhat lower than two-thirds power of the mass ratios. An inspection of 14 electric vehicles detailed in Ref 32 indicates that approximately

$$\left(\frac{FA'}{FA}\right) = \left(\frac{VM'}{VM}\right)^{1/2} \quad (20)$$

or

$$FA' = FA \left(\frac{VM'}{VM}\right)^{1/2} \quad (21)$$

where FA' represents the changed frontal area caused by a corresponding increase or decrease in vehicle mass VM'.

Axle and Transmission Characteristics

Energy losses in the conventional automotive rear axle occur from relatively speed-insensitive sources such as oil seal and bearing preload drag as well as from speed-sensitive lubrication viscous drag. Due to the popular use of hypoid ring and pinion gear sets to provide a lowered drive-shaft offset, sliding gear viscous losses make the typical rear axle somewhat less efficient than a bevel-gear set or chain drive (Ref 42). Since certain losses are relatively constant (e.g. seal drag), axle efficiency, defined by

$$\eta_A = \frac{P_{IN} - \text{losses}}{P_{IN}} \cdot 100 \quad (22)$$

where P_{IN} is the input power to the pinion shaft, becomes a function of input power as well as speed. Figure 2 shows an experimentally obtained typical axle efficiency map (Ref 1). Note that the abscissa coordinate is percent of rated input power, indicating that, generally, maximum efficiency occurs with minimally sized components. A least-squares quadratic fit of the data represented by Fig 2 yields the following:

$$\eta_A = 95.8 - \frac{.01217(PSPD)^2 + .8879(PSPD) + 4.261}{PP} \quad (23)$$

where PSPD and PP are percent rated speed and percent rated input power respectively. Eq (23) is a very accurate fit to the data on Fig 2 with

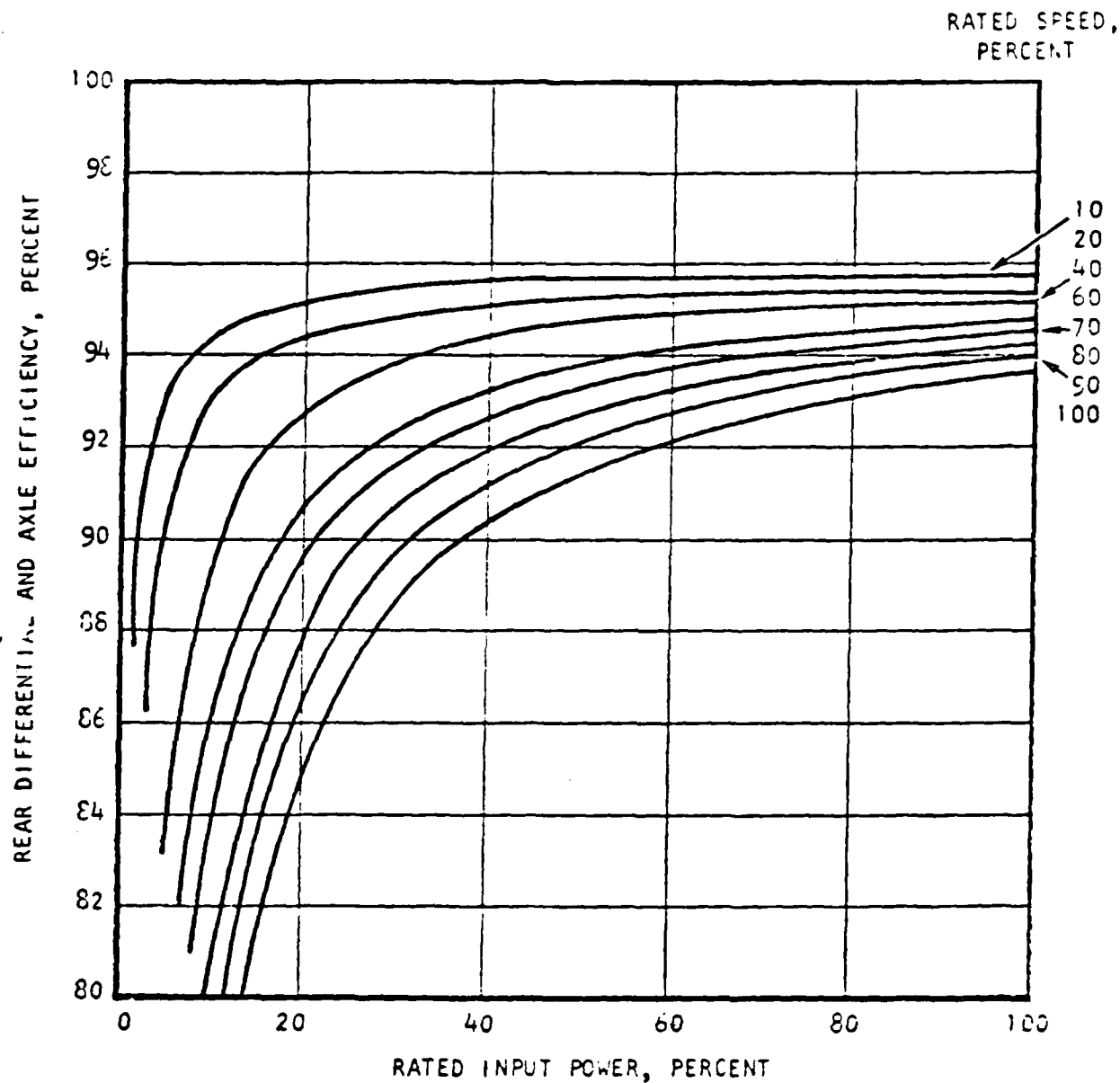


Fig 2. Rear Axle Efficiency

errors of less than .2 percent at all power levels above 15 percent.

Conventional fixed-ratio multi-speed transmissions have efficiency maps very similar to that of a rear axle (Fig 3). Since hypoid gears are not used, however, the sliding friction component is reduced, and consequently straight spur or helical-cut transmission efficiencies are considerably less speed dependent. The efficiency is dependent, however, on the reduction ratio with 1:1 being the most efficient. Maximum efficiencies are reported to vary from 99 percent at 1:1 ratio to 94.5 percent at 2.55:1 (Ref 28). These maximum efficiencies can be closely approximated with the following exponential equations as functions of gear ratio GR:

$$\eta_{MAX} = 99e^{-0.03(GR-1)} \quad (24)$$

for gear ratios greater than 1:1, or

$$\eta_{MAX} = 99e^{-0.03(1-GR)} \quad (25)$$

for overdrive ratios (i.e. gear ratios less than 1:1). As with the rear axle efficiency derivation, a least-squares quadratic fit of a published transmission efficiency map (Ref 1) yields an accurate equation in terms of percent rated shaft speed PSPD_T, percent rated input power PP, and maximum efficiency η_{MAX} . This equation, to be used with Eqs (24) or (25) is

$$\eta_T = \eta_{MAX} \left(99 - \frac{.00405(PSPD_T)^2 - .1849(PSPD_T) + 1.565}{PP} \right) \quad (26)$$

A variety of variable-ratio transmissions have been suggested for use with electric vehicles (Refs 2, 3, 19, 32, 36, 37). These include infinitely-variable roller traction drives, hydrostatic drives, and continuously-variable belt drives. Due to the nonlinearities and peculiarities associated with each of these non-standard transmissions, no attempt was made to "close-fit" an efficiency equation for each case. Instead, this model uses their efficiency data stored in the form of a tabular two-dimensional performance map with dependent variables of speed ratio and percent rated input power. A look-up procedure is then used with two-dimensional linear interpolation when appropriate.

Motors

For reasons mentioned in Chapter I, this vehicle model considers only DC motors. However, both series and shunt motors are candidates and, as such, are individually represented. Compound motors (with both shunt and series field windings) are not modeled, but depending upon the relative series compounding ratio, may be compared with the behavior of a similarly-sized series or shunt motor. The essential requirement of any motor model is to be able to relate output power and current for any operating speed or applied voltage.

Series Motor. In series motors, the armature current I_a passes entirely through the field circuit. Figure 4 shows a simplified circuit analysis model.

The complete voltage equation for Figure 4 is

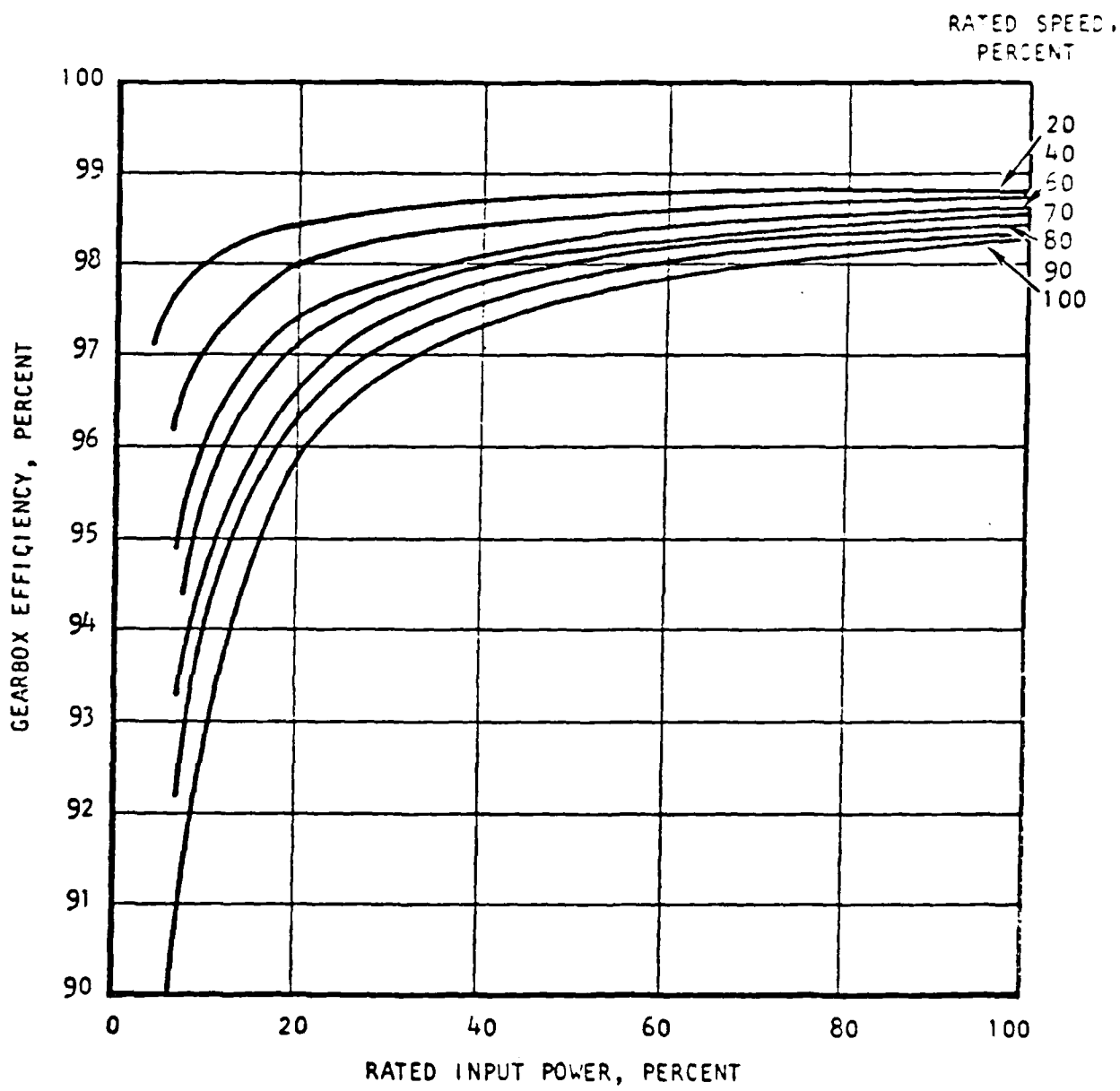


Fig 3. Gear Ratio Transmission Efficiency

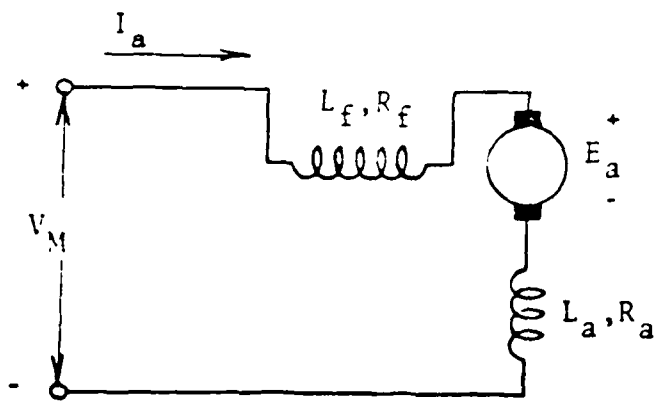


Fig 4. Series Motor Diagram

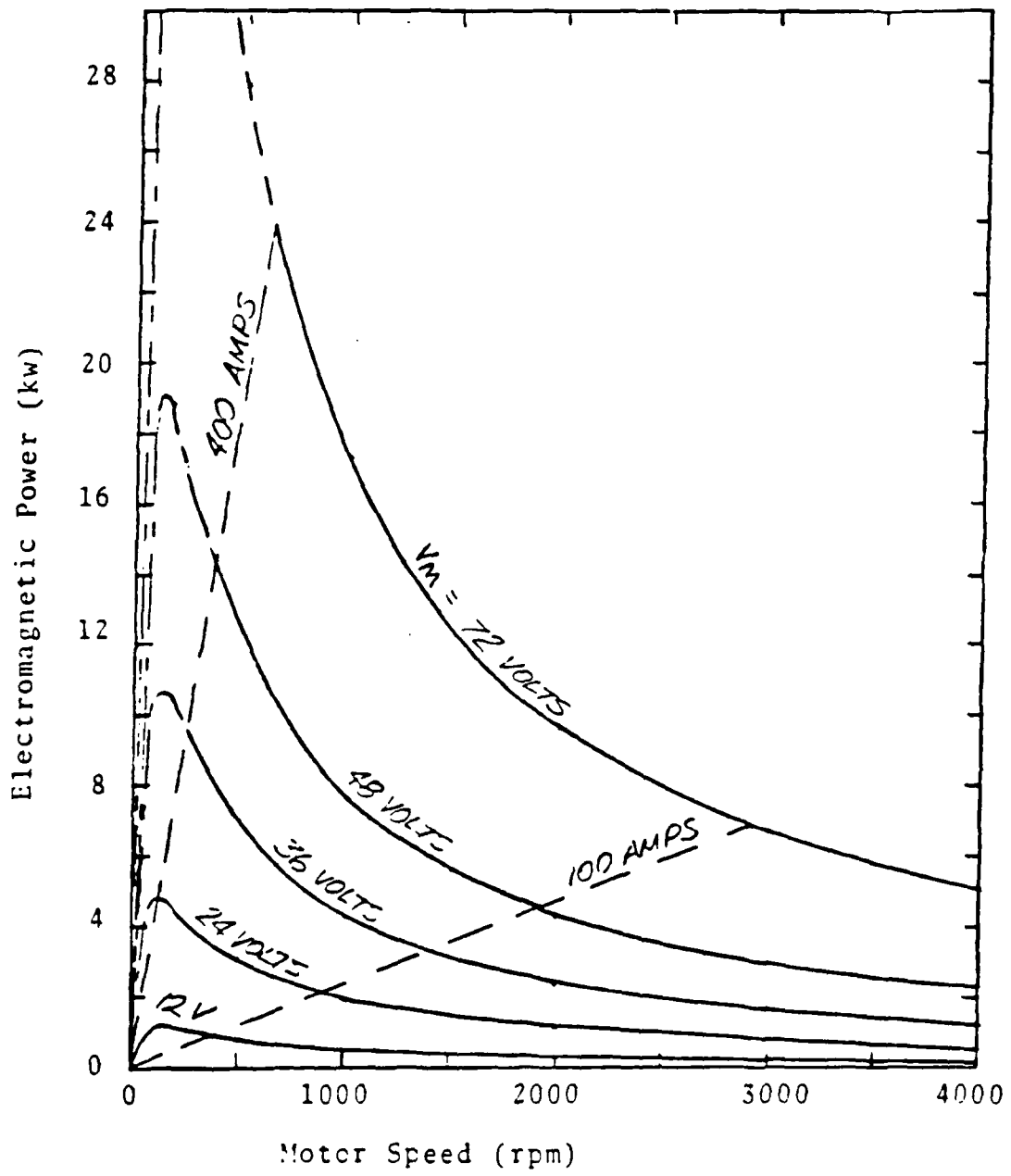


Fig 5. Series Motor Performance

$$V_M = I_a (R_f + R_a) + E_a + (L_f + L_a) \frac{dI_a}{dt} \quad (27)$$

where L_f and L_a are the field and armature inductances, V_M is the applied motor voltage, and E_a is the induced center-electromagnetic force (EMF) in the armature. The dynamic inductance terms at the end of Eq (27) are significant only for very short intervals of rapid current change and for this analysis can be ignored (Ref 27). Electromagnetic power of the motor is defined as the input electrical power minus all I^2R copper losses. This can be revealed by multiplying both sides of the steady-state version of Eq (27) by I_a and rearranging the terms

$$E_a I_a = V_M I_a - I_a^2 (R_f + R_a) \quad (28)$$

From the driving cycle, which determines transmission and controller position, the motor speed n and V_M can be determined. Thus the variables on the right side of Eq (28) must be further reduced into functions of only n and V_M to obtain an equation of power useful in the simulation. Solving for I_a , again using the steady state Eq (27), results in

$$I_a = \frac{V_M - E_a}{R_f + R_a} \quad (29)$$

The counter EMF is proportional to the field strength ϕ and motor speed. For series motors, assuming a linear magnetization curve (i.e. unsaturated fields), ϕ is proportional to I_a . Thus, from Eq (29)

$$I_a = \frac{V_M - nk\phi}{R_f + R_a} \quad (30)$$

or

$$I_a = \frac{V_M - nk*I_a}{R_f + R_a} \quad (31)$$

where $k*$ is a new combined proportionality constant. Separating the armature current terms from Eq (31) and simplifying results in

$$I_a = \frac{V_M}{R_f + R_a + nk*} \quad (32)$$

which has the necessary V_M and n dependence for reinsertion into Eq (28). The electromagnetic power is finally then

$$E_a I_a = \frac{V_M^{nk*}}{(R_f + R_a + nk*)^2} \quad (33)$$

Equations (32) and (33) may be combined to develop an overall motor performance map as is shown in Fig 5 for a typical series motor. The essential series motor characteristics of high torque (i.e. power) at low speed and theoretical unlimited no load speed can be seen from this figure. The actual operating envelope of any motor is limited by the applied voltage (somewhat less than nominal battery voltage, see Battery

Model, this chapter) on one side and by the maximum allowable armature current on the other. Depending upon the robustness of the individual series design, manufacturers' recommended maximum currents are from two to five times the normal current at rated power and speed (Refs 4, 13).

Shunt Motors. The armature current in a shunt field motor does not pass through the field circuit; in fact, for maximum flexibility, the field is often separately excited as shown in Fig 6. Neglecting the dynamic inductance voltages as before, the steady state circuit voltage equations are:

$$V_a = E_a + I_a R_a \quad (34)$$

$$V_f = I_f R_f \quad (35)$$

where V_f and I_f refer to the separate field circuit. Similarly to the series motor, the electromagnetic power equation may be developed from Eqs (34) and (35). In this case, however, the field flux ϕ is proportional to the field current which from Eq (35) equals V_f / R_f . The final steps in the derivation result in

$$I_a = \frac{V_a - nk^* \left(\frac{V_f}{R_f} \right)}{R_a} \quad (36)$$

$$E_a I_a = \frac{nk^* V_f}{R_a R_f} \left\{ V_a - nk^* \left(\frac{V_f}{R_f} \right) \right\} \quad (37)$$

The shunt motor performance map on Fig 7, developed from Eqs (36) and (37) where $V_f = V_a$, illustrates the need for separate field control with shunt motors to improve low speed performance and speed flexibility. Again the operating envelope is limited by available voltage and maximum allowable armature current. Typically, shunt armature currents should not exceed two or three times the rated value to prevent commutation problems and overheating (Refs 4, 13).

Common Parameters. The motor constants R_a , R_f , and k^* in Eqs (33) and (37) must be resolved into functions of the motor's power rating P_r to provide the simulation with the ability to rescale the motor to meet any particular design criteria. The following relations were developed for modeling motors of different P_r with the same rated voltage and speed:

$$\frac{I_a'}{I_a} = \frac{P_r'}{P_r} \quad (38)$$

$$\frac{k^*'}{k} = \frac{R_a'}{R_a} = \frac{R_f'}{R_f} = \frac{P_r'}{P_r} \quad (39)$$

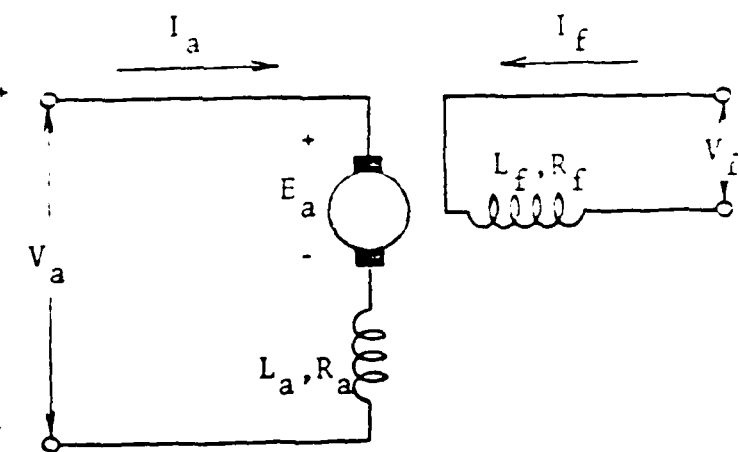


Fig 6. Separately Excited Shunt Motor Diagram

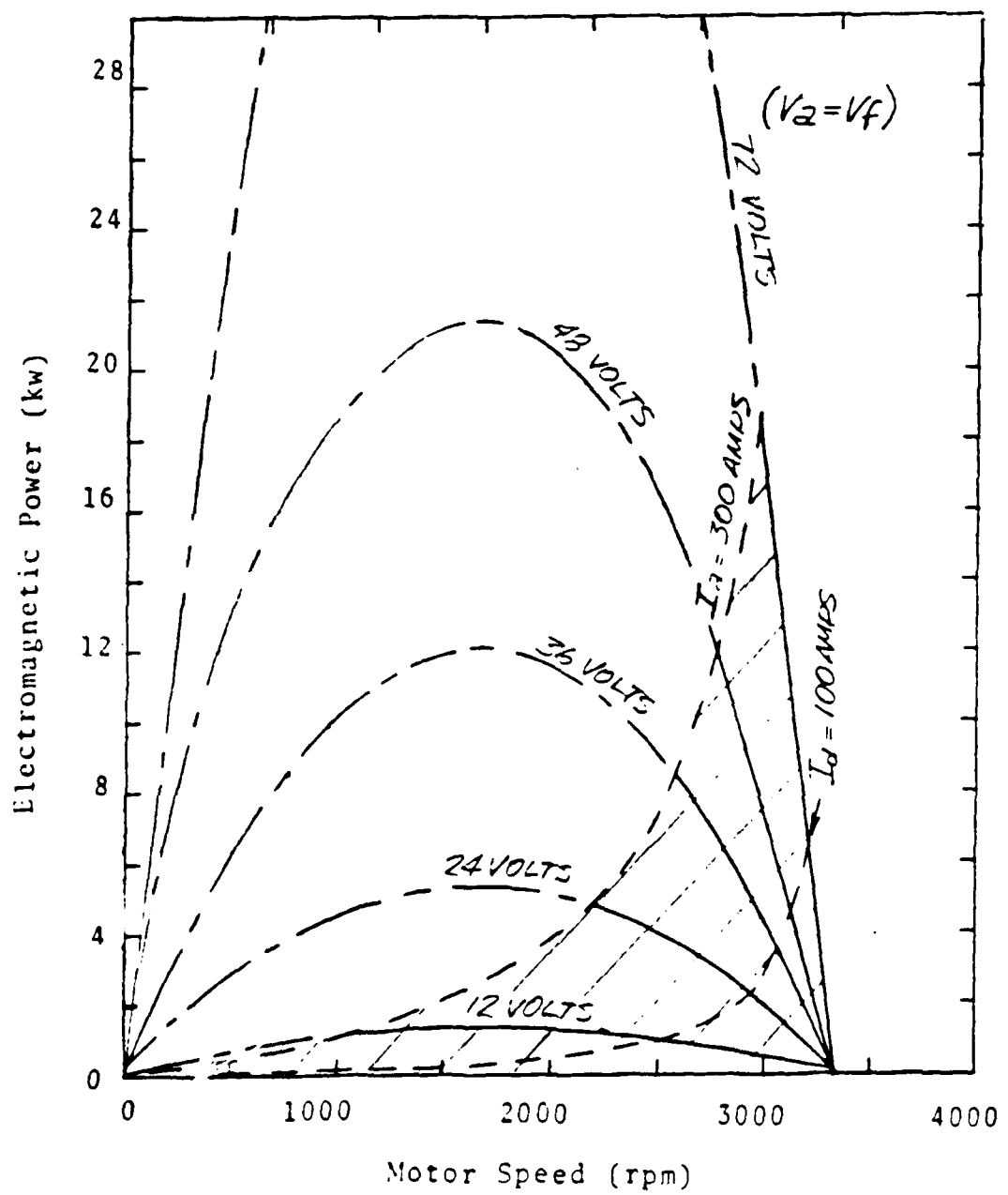


Fig 7. Shunt Motor Performance

where the prime superscript denotes changed values over the basic P for which k^* , r_a , R_f , and I_a for any operating condition are known (Ref 41).

To this point, all motor performance has been based on available electromagnetic power, $E_a I_a$. Additional mechanical losses and stray-load losses reduce the actual power output to some fraction of the $E_a I_a$ (Ref 4). These losses include bearing and brush drag, rotor windage, field hysteresis and eddy current-induced heating. The total effect is an involved function of motor speed, voltage, and current and is difficult to establish analytically. Available experimental data are in the form of overall motor efficiency curves which relate net output power to electrical input power $V_M I_a$. The motor model for this simulation uses motor efficiency data η_M stored in tabular form as described in Appendix D to obtain net output power P_{OUT} from the calculated $E_a I_a$ by the following equations:

$$P_{OUT} = \{E_a I_a + I_a^2 (R_a + R_f)\} \eta_M \quad (40)$$

for series motors or

$$P_{OUT} = \{E_a I_a + I_a^2 R_a + I_f^2 R_f\} \eta_M \quad (41)$$

for shunt motors.

The final motor parameter required for complete modeling is mass MM as related to P and rated speed n_r . For constant voltage and speed ratings, the amount of active magnetic material in the field and armature determines the torque (hence, power) of a motor. Reference 27 suggests that a logarithmic relationship generally exists between motor mass and power rating. Indeed, a graphical analysis of manufacturer's data (Ref 13) reveals the following relationship between 3200 rpm rated motors:

$$MM = \{5.75 \log(P_r)\} 21.5 \quad (42)$$

A similar logarithmic relation exists between equal powered motors rated at different speeds. Again, analysis of data from Ref 13 provides the following version to Eq (42) for motors rated at other than 3200 rpm:

$$MM = \{5.75 \log(P_r)\} 21.5 \{ .162 \log(\frac{n_r}{3200}) \} \quad (43)$$

Controllers

Motor controllers must regulate the motor voltage to adjust power output and limit armature current at low speeds. To be satisfactory, they must accomplish this control with minimum power loss.

Step-Voltage Switching. Motor controllers which employ mechanical relays to adjust the parallel-series battery network dissipate power only through the relay activator circuits and slight contact resistance. Properly designed, their efficiencies can exceed 99 percent (Ref 32). Ignoring this negligible power loss, modeling consists of simply knowing the battery voltage fraction available at each step and the corresponding parallel-series network. Analysis of the net source impedance requires this know-

ledge of the specific battery arrangement for each step. Since the number of individual relays required increases dramatically with the number of steps provided (e.g. nine relays for three steps, 21 relays for four steps, (Ref 30), the practical upper limit for these controllers is three.

To accommodate additional voltage steps while reducing the relay requirement, high current diodes may be inserted to replace selected relays. The simplicity and economy they offer over relays is partially balanced by the losses they create. Depending upon the semi-conductor material used in their construction, these diodes will typically produce about a one-volt drop when normally conducting with forward bias. Discriminate placing of these diodes minimizes their dissipative losses by requiring only a fraction of the total current to pass through any single diode. The net effect on the switching controller model by the addition of diodes is to lower each step's voltage fraction by the appropriate diode-induced voltage drop.

Solid-State Inverters (Choppers). Electronic chopper controls offer continuous voltage control from zero to 95 percent of the battery voltage. Their basic principle is to switch the motor on and off at a high frequency (up to 1000 Hz) while controlling the relative duration of the conduction and nonconduction periods to produce varying time-averaged voltages. The power losses associated with choppers result from the resistive and semi-conductor elements used in the oscillator circuits. The combined losses have been modeled (Ref 2) as

$$P_C = (1.5 \text{ volts})I_M + (.03)E_a I_a \quad (44)$$

where the first term on the right side is the semi-conductor junction loss and the second term, the resistive losses as a function of motor power. These losses can be more easily accounted for when referred back to a voltage drop. Dividing Eq (44) by the supply current, assuming that $I_M = I_a$ and that $E_a \approx V_M$, results in

$$V_C = 1.5 + .03V_M \quad (45)$$

This controller loss then reduces the net instantaneous battery voltage V_B available to the motor since

$$V_M = V_B - V_C \quad (46)$$

or combining Eqs (45) and (46)

$$V_M = \frac{V_B - 1.5}{1.03} \quad (47)$$

Batteries

While numerous battery types promising badly-needed energy and power density improvements lead-acid batteries with their commercial availability and proven reliability form the basis for this battery model. The model could be modified for alternate battery types by substituting the appropriate performance parameters. Currently, however, insufficient published experimental data are available to detail the dynamic performance of these

batteries, although the Shepherd Equation (Refs 38, 39), with its empirically-derived constants, provides some insight. Any useful battery model must be able to predict power available and energy remaining at any time during a driving cycle as functions as battery mass, ambient temperature, discharge level, load current, nominal voltage, and loading history.

Energy Capacity. The constant load useful capacity of a battery is a function primarily of discharge rate. Figure 8 shows the constant load capacity characteristics (Ref 32) used in this model. A least-squares quadratic approximation of that data results in

$$c = 195 - .633(I_B) + 9.13 \cdot 10^{-4}(I_B)^2 \quad (48)$$

where battery capacity c is expressed in amp-hrs and I_B is the steady battery discharge current. The capacity of lead-acid batteries is also a strong function of temperature (Ref 43). Eq (48) is correct only for the standard test temperature of 25 C. For other temperatures, the capacity is modified by factor c^* , where

$$c^* = .014(T) + .65 \quad (49)$$

Incorporating this into Eq (50) results in

$$c = \{195 - .633(I_B) + 9.13 \cdot 10^{-4}(I_B)^2\} \cdot \{.014(T) + .65\} \quad (50)$$

Eq (50) is still only correct for constant I_B values. An incremental scheme based on sequentially solving this equation for each incremental value of I_B would yield an incorrect total discharge value.

During discharge of any battery with liquid electrolyte, ion migration toward their respective electrodes within each cell causes the output to be time-dependent (Ref 38). This developed non-homogeneity, in effect, temporarily reduces the capacity of the battery. Under lighter loads or no load, the electrolyte eventually redistributes itself homogeneously again. The consequence of this time-dependent characteristic is that the instantaneous capacity of a battery is a strong function of previous discharge rate as well as present load. Likewise, idle time actually provides a recuperative effect to marginally regain capacity. The following discharge equations consider load history in terms of average current \bar{I}_B and have shown good correlation with experimental results (Ref 6):

$$DF = \left\{ \frac{\bar{I}_B \cdot t}{c} \left(\frac{I_B}{\bar{I}_B} \right) + \frac{I_B \cdot t}{c} \left(1 - \frac{I_B}{\bar{I}_B} \right) \right\} 3600 \quad (51)$$

for instantaneous current $I_B <$ average current \bar{I}_B or

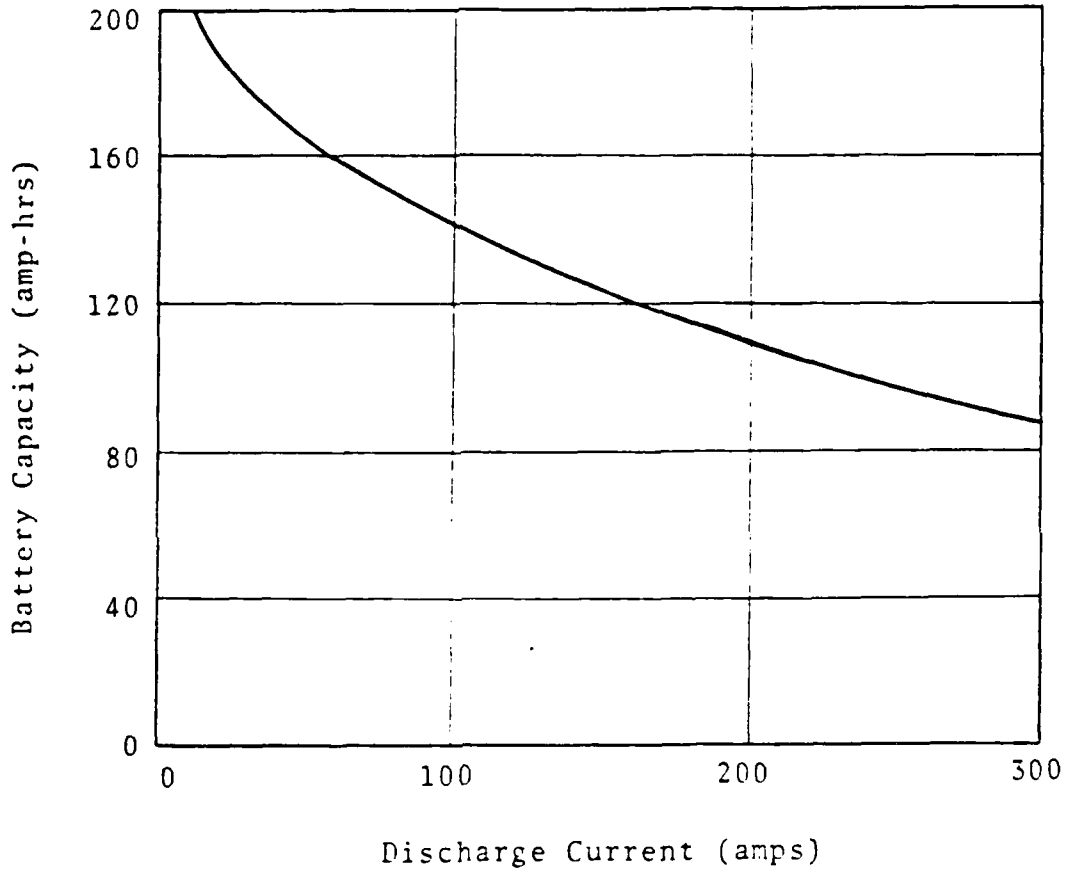


Fig 8. Lead-Acid Battery Discharge

$$DF = \left\{ \frac{\bar{I}_B \cdot t}{c} \frac{\bar{I}_B}{\bar{I}_B} + \frac{\bar{I}_B \cdot t}{\bar{c}} \left(1 - \frac{\bar{I}_B}{\bar{I}_B}\right) \right\} 3600 \quad (52)$$

for $I_B > \bar{I}_B$. The discharge fraction DF represents the accumulated portion of the battery used during the cycle time t while c and \bar{c} are the solutions to Eq (50) based on I_B and \bar{I}_B respectively. Since Eq (50) was developed from data for a single standard size (~ 29 kg), six-volt, golf-cart style battery, any simulated change in battery mass must appropriately affect the discharge life. This model assumes that increased battery mass results in the addition of electrode plate area, hence the current I_B in Eqs (51) and (52) may be replaced by a current I_B' such that

$$I_B' = I_B \left(\frac{BM}{BM'} \right) \quad (53)$$

where BM' is the new battery mass and BM is the nominally-sized mass based on the batteries characterized by data given in Fig 9.

Available Power. The output of a battery is equal to its output voltage times the load current. The load current is a function of the vehicle demands while the output voltage depends upon that current as well as the instantaneous discharge state of the battery and electrolyte temperature. For constant temperature, the battery's volt-amp characteristic may be modeled as a constant resistance (Ref 1, 32, 38, 43). For the lead-acid type considered, this resistance R_B is assumed to be .003 ohms per standard six-volt battery at 25 C. As with capacity, this resistance value is also a function of temperature (Ref 43). A quadratic approximation of this temperature dependence produces the following equation for relative resistance R_B^* :

$$R_B^* = (.00087)T^2 - (.047)T + 1.63 \quad (54)$$

Hence the overall resistance per battery is

$$R_B = (.003)R_B^* \quad (55)$$

Battery connector cable impedance is not explicitly modeled since properly sized wire with short lengths will keep this value an order of magnitude below the battery resistance. However, when significant, this resistance may be added to Eq (49).

A final consideration in the voltage profile of a battery is the present stage of discharge. In general, the voltage produced at any temperature and load will decrease as the battery becomes increasingly discharged. For this model, in fact, 100 percent state-of-discharge is defined as when the cell potential has dropped to 1.75 volts at a steady load of 80 amps. This definition, combined with typical lead-acid discharge characteristics (Refs 1, 14), results in the following equation for no-load cell voltage:

$$V_c = 2.03 + (.08)DF - (.28)DF^2 \quad (56)$$

Including resistance effects (Eq 49), the general voltage expression for a nominal six-volt battery thus becomes:

$$V_B = 6.09 - (.003)R_B^*I_B + (.24)DF - (.84)DF^2 \quad (57)$$

To model a change in battery mass, the nominal resistance R_B is replaced by a new value R_B' related to the BM change by

$$R_B' = R_B \left(\frac{BM}{BM'} \right) \quad (58)$$

where BM' is again the new battery mass.

An added consideration for a useful battery model is the net battery efficiency. This is defined as the ratio of energy discharge to the charging energy (Ref 22). Therefore, this efficiency is a function not only of discharge rate and extent, but also the charging rate and extent of charge. In general, high discharge and charge rates lower the efficiency due to internal resistance losses and hydrogen gas formation. However, the most efficient rate of charge varies directly with the battery's depth of charge. Also, due to internal polarization, some experimental evidence indicates that high charging rates immediately following high discharge rates can be very efficient (Ref 1). In view of the complexity of dynamically modeling both charge and discharge cycles, this battery model uses an experimentally derived (Ref 32) average efficiency of 70 percent.

Hybrid Power. As discussed in Chapter I, the major utility of gas-powered hybrid augmentation is to relieve battery drain during high speed cruise. For that reason, the hybrid is modeled as being inactive until a designated engagement speed. At that speed the hybrid becomes positively connected to the motor shaft via some transmission arrangement and is capable of producing any power up to the maximum for its particular operating speed. The hybrid engine currently included in the vehicle model is a 7.5 kw, two-cycle industrial engine (Ref 45). From published performance curves, the maximum power available from this hybrid engine is:

$$P_H = \{(8.7 \cdot 10^{-4})n_H + .99\}n_H \quad (59)$$

where the engine speed n_H equals the motor speed multiplied by the hybrid transmission ratio and η_H is the average power efficiency of that transmission. The fuel consumption of the engine is also taken from manufacturer's data (Ref 23) and is modeled as a constant brake-specific fuel consumption of .56 liters per kwh.

This final entry now completes the vehicle model characteristics required to obtain the net input energy necessary to meet the driving cycle road load power demands. It remains for the simulation then to combine all the dynamic characteristics of a particular vehicle system with a driving and speed schedule to derive the instantaneous and overall vehicle performance.

III. Simulation Methodology

Figure 9 is a simplified flow chart of the simulation program EVSIM developed during this effort. Reference 41 includes a user's guide and includes a sample computer listing, data deck, and sample output. Additional information on two of the more involved subroutines, VSTEP and TRANSEFF, are also located in Reference 41.

The simulation begins by selecting certain "fixed" vehicle and environment parameters. These represent a particular vehicle type and surrounding influences and include such things as payload mass, transmission type, and motor type as well as ambient temperature and fuel costs. Certain "basic" vehicle parameters are also entered at the start. These are parameters such as motor power and battery mass which may be incrementally changed by the simulation to meet specific performance criteria. Table II lists all the specific input parameters grouped by their category.

An input driving cycle is needed to provide a second-by-second speed schedule. For each time increment, road load forces are calculated and converted to power required at the wheels. Through continuous efficiency equations and/or component efficiency maps, this raw road power is converted to the required motor output power. Calculation of the available motor power depends upon the controller type. For step-type controllers, only discreet power steps are available for any particular motor speed (Reference 41); hence, an exact match with the required power at any increment is unlikely. The power step closest to the power required is selected and then an iterative procedure accomplished by adjusting the interval's terminal speed until the power required does match the available power. For continuous controllers, EVSIM assumes a perfect match between required and available power until the maximum available power is insufficient to meet the demands. Then, as with the step-controller an iterative procedure determines the actual speed attained at the end of each interval. For systems using a gas-engined parallel hybrid, the simulation assumes that the continuously controllable hybrid power is used only to match the total available power with that required.

Once the actual vehicle speed and motor power for each time increment have been resolved, the fraction of battery discharge is calculated. This entire process is repeated until the cycle is complete or until the vehicle fails to meet some minimum critical performance criterion. If the basic vehicle is insufficiently powered, an excessive speed deviation from the driving cycle schedule will cause EVSIM to increase the rated power and associated parameters until the schedule can be achieved. On the other hand, if lack of energy storage is apparent from an excessive discharge fraction, EVSIM can increase the battery mass. Naturally, both of these parameter adjustments are interrelated and typically one will require the other.

When the input driving cycle has been successfully completed the final outputs of EVSIM include the total motor energy used, the total deceleration energy available at the motor (for regeneration), the percent of battery discharge at cycle completion, the average electrical cost per kilometer, and the final vehicle parameters if adjustments were made. The power cost is based on an average charger efficiency of 85 percent (Reference 32) combined

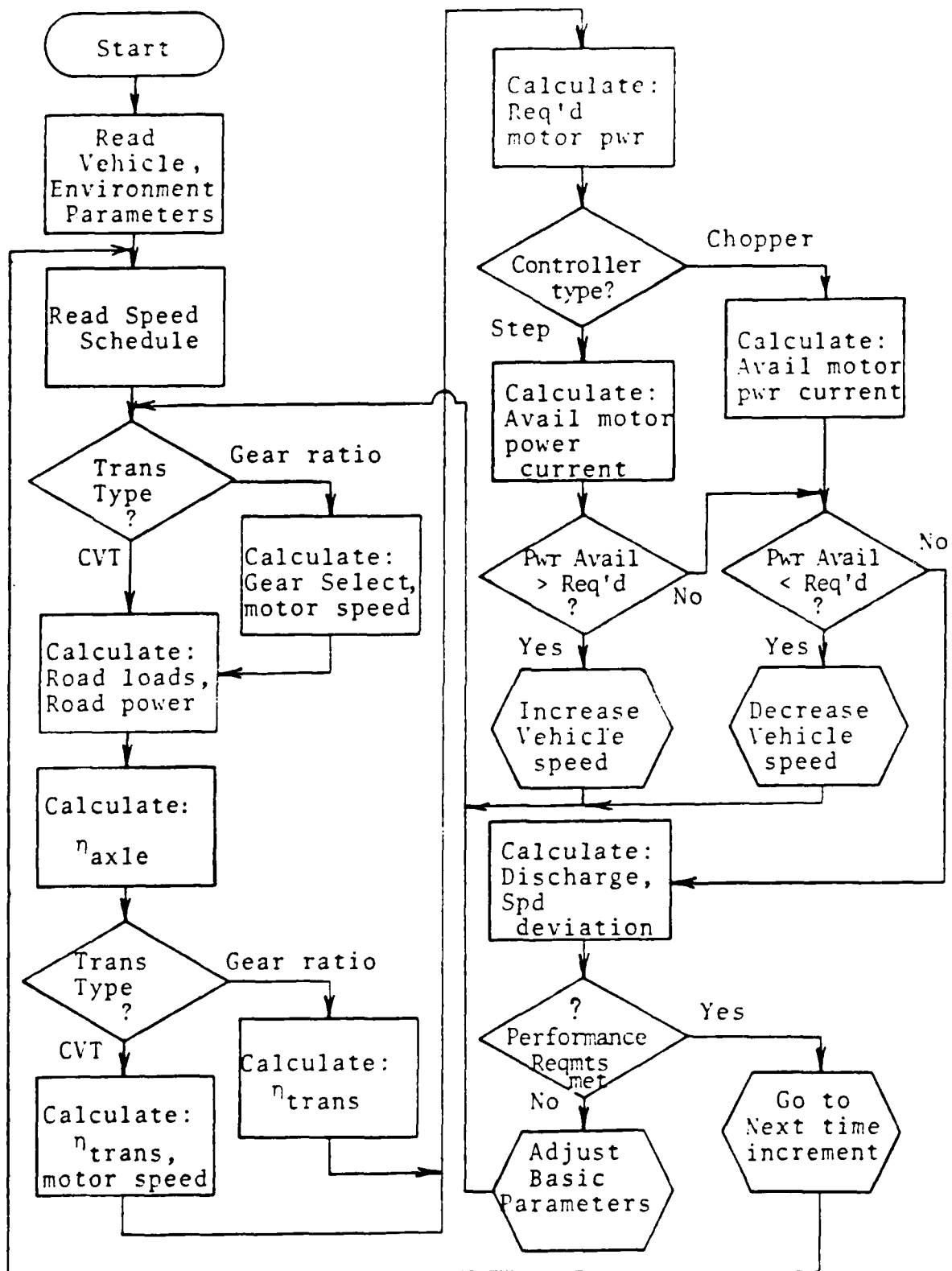


Fig 9 EVSIM Flow Chart

with the battery model's 70 percent efficiency to produce a net 60 percent energy transfer from AC power at the charger to DC power out of the batteries. If a parallel hybrid system is simulated, EVSIM also recalls the total engine energy used along with the average petroleum fuel cost per kilometer.

TABLE II
EVSIM Input Parameters

	FIXED	BASIC
Vehicle Parameters	Drag coefficient	Frontal area
	Payload mass	
	Fixed mass	
	Rolling radius	
	Rolling coefficient	
	Axle ratio	
	Transmission type (Multi-ratio) gear ratios shift speeds (CVT) efficiency data	
	Motor type base speed efficiency data maximum power ratio	Rated power Armature resistance Field resistance k* value Maximum current
	Controller type (Step voltage) voltage fractions	Step source impedance
	Nominal battery voltage Hybrid coupling efficiency speed ratio engagement speed operating gear	Battery mass
Other Parameters	Ambient temperature Electric energy cost Petroleum fuel cost Speed schedule Program option	

Input Driving Cycle

A critical feature in any vehicle simulation is the realism of the driving sequence. Several test cycles have been devised for both conventional and electric vehicles. While the more elaborate cycles more accurately represent actual driving experiences, the tradeoff is the increased difficulty in simulating these sequences and, consequently, obtaining vehicle road loads.

Cycle Selection

In February 1976 the SAE J227a Electric Vehicle Test Procedure was developed. This cycle was designed primarily for track testing and was produced in three versions, the most demanding of which is shown in Figure 1D. This schedule, with its top speed of 72 km/hr, is most frequently used to simulate "variable-route suburban" driving. As only the end points of each portion are specified, distinct acceleration or deceleration profiles are not required. The relative ease of simulating this driving cycle has led to its frequent use (References 1, 9, 19, 32, 37). However, when used in track tests (Reference 32), it generally overpredicts range and underestimates energy usage rate when compared to user experience.

A much more intricate driving cycle is the Federal Urban Driving Sequence (FUDS, Reference 10), which was developed primarily for dynamometer vehicle emission tests. It is, however, also used by the Environment Protection Agency for new car urban fuel economy tests. This 23-minute cycle is the recorded operation of an actual vehicle being driven in the Los Angeles area. As such, it is a second-by-second speed schedule that includes frequent stops, random traffic-induced speed adjustments, and one short stretch of 90 km/hr freeway travel (Figure 11). In spite of its complexity (1371 data points), its realism and ability to provide a base for operating cost comparison with new conventional vehicles made the FUDS the logical choice for this simulation.

Simulation Output

The sample output on Figure 12 demonstrates EVSIM's evaluation mode. The vehicle modeled has the configuration of the test-bed vehicle design. It represents a series motor/gasoline engine parallel hybrid. The transmission is a four-speed conventional gear ratio model (although only the first three gears are used during hybrid augmentation). The controller is a five-step battery-switching system that uses a combination of relays and high power diodes to control the motor supply voltage. The selected portions of the complete cycle included in Figure 12 indicate the extent of computed data available for each increment of the chosen driving cycle. The final page of sample output shows the overall energy recap that is computed at the end of each completed simulation cycle.

EVSIM's cruise sequence at a constant 88 km/hr is demonstrated in Figure 13. The same performance and energy use summary is presented following the complete discharge of the batteries.

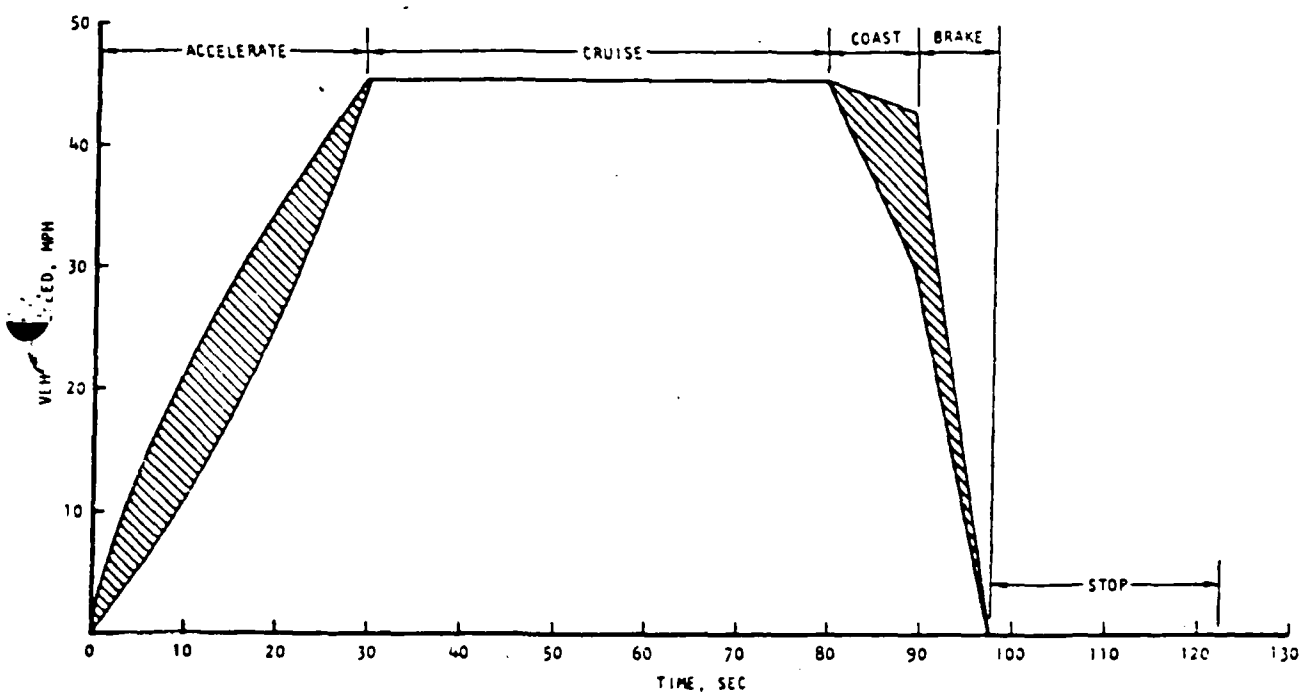


Fig 10 SAE J227a Test Cycle

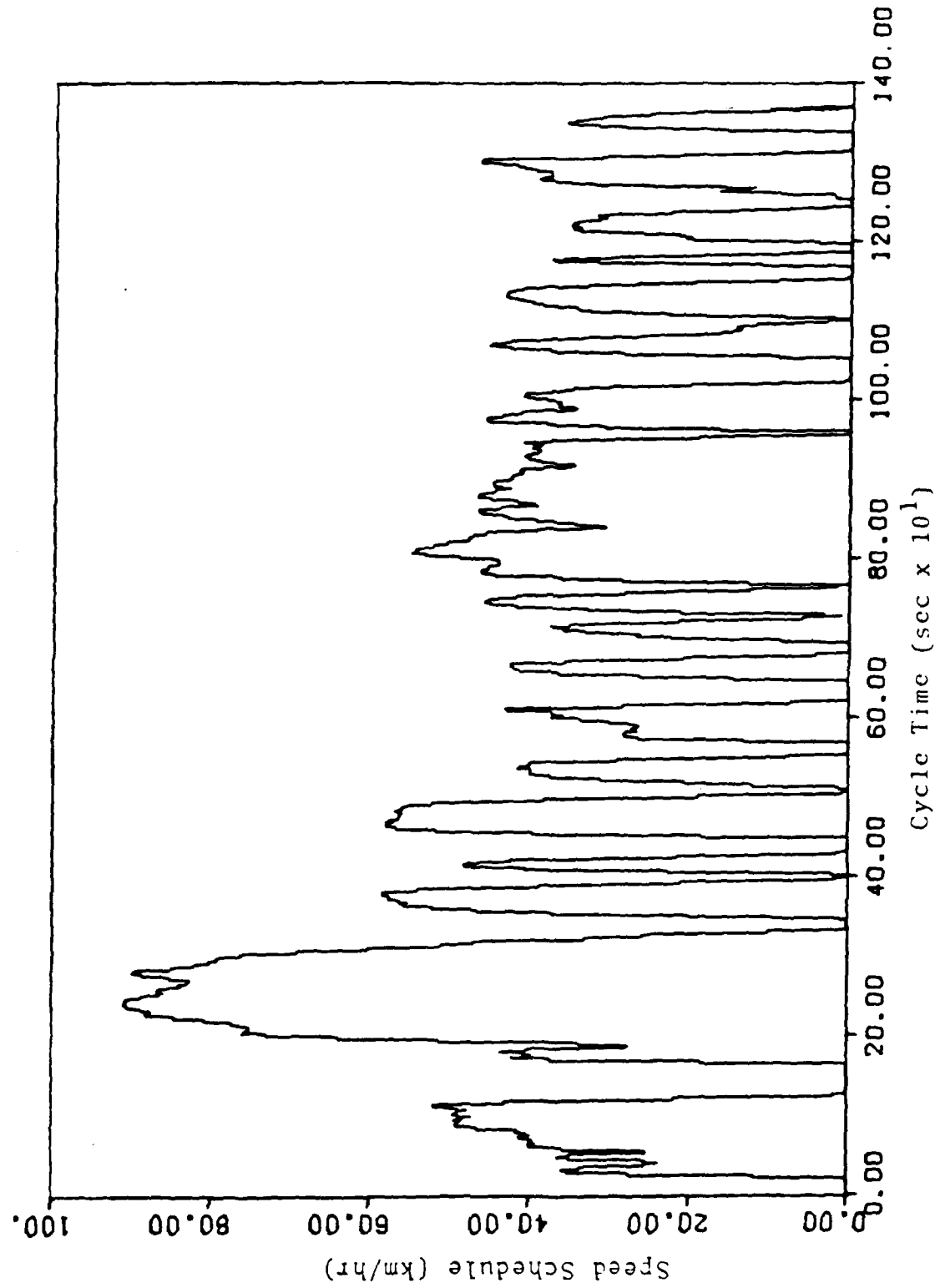


Fig 11 Federal Urban Driving Sequence

*** ELECTRIC VEHICLE SIMULATION ***

VEHICLE CONSTANTS ARE:

DRAG COEFFICIENT= .42
FRONTAL AREA= 1.80 SQUARE METERS
PAYLOAD MASS=270. KILOGRAMS
FIXED MASS=325.

ENVIRONMENTAL CONSTANTS ARE:

AMBIENT TEMPERATURE= 27. CELSIUS
ELECTRIC ENERGY COST= \$.050 PER KWHR
PETROLEUM FUEL COST= \$.35 PER LITER

POWER REDUCTION VARIABLES ARE:

TIRE ROLLING RADIUS= .343 METERS
ROLLING COEFFICIENT= .0105
AXLE RATIO= 4.13
NUMBER FORWARD GEARS= 4
MAXIMUM VELOCITY=112. KM/HR

FIXED SPEED TRANSMISSION VARIABLES ARE:

MOTOR UPSHIFT SPEED=1500. RPM
MOTOR DOWNSHIFT SPEED= 500. RPM
GEAR RATIOS= 3.800
2.060
1.260
.880

MOTOR VARIABLES ARE:

MOTOR TYPE= SERIES
RATED POWER= 6.0 KW
BASE SPEED=3200. RPM
MAX ARMATURE CURRENT= 400. AMPS

5 STEP CONTROLLER VARIABLES ARE:

VOLTAGE FRACTION= .167	SOURCE IMPEDANCE= .0030 OHMS
.333	.004
.500	.009
.667	.018
1.000	.036

BATTERY VARIABLES ARE:

INITIAL VOLTAGE= 72.
BATTERY MASS= 350.

7KW SERIES HYBRID VARIABLES ARE:

HYBRID/MOTOR SPEED RATIO= 1.950
COUPLING EFFICIENCY= 96.5%
ENCACEMNT SPEED= 45.0KM/HR
TRANSMISSION POSITION= 3 GEAR

SYSTEM EVALUATION OPTION SELECTED

Fig 12 EVSIM Sample Output

TIME	VELOC-ICP (sec)	VELOC-ACT (KMP/HRS)	DEVIATION (KMP/HRS)	F-ROLL (NT)	F-AIR (NT)	F-ACCEL (NT)	INPUT-POWER (PTR) (HYD)	GEAR SELECT (PTR) (HYD)	SHT-RPM STEPFIELD	PIN	PIN AMPS	BAT DISCHARGE Amp
1	0.0	0.0	0.0	131.	0	0.0	0.0	0	0	C-0	0	0.0000
2	0.0	0.0	0.0	131.	0	0.0	0.0	0	0	C-0	0	0.0000
3	0.0	0.0	0.0	131.	0	0.0	0.0	0	0	C-0	0	0.0000
4	0.0	0.0	0.0	131.	0	0.0	0.0	0	0	C-0	0	0.0000
5	0.0	0.0	0.0	131.	0	0.0	0.0	0	0	C-0	0	0.0000
6	0.0	0.0	0.0	131.	0	0.0	0.0	0	0	C-0	0	0.0000
7	0.0	0.0	0.0	131.	0	0.0	0.0	0	0	C-0	0	0.0000
8	0.0	0.0	0.0	131.	0	0.0	0.0	0	0	C-0	0	0.0000
9	0.0	0.0	0.0	131.	0	0.0	0.0	0	0	C-0	0	0.0000
10	0.0	0.0	0.0	131.	0	0.0	0.0	0	0	C-0	0	0.0000
11	0.0	0.0	0.0	131.	0	0.0	0.0	0	0	C-0	0	0.0000
12	0.0	0.0	0.0	131.	0	0.0	0.0	0	0	C-0	0	0.0000
13	0.0	0.0	0.0	131.	0	0.0	0.0	0	0	C-0	0	0.0000
14	0.0	0.0	0.0	131.	0	0.0	0.0	0	0	C-0	0	0.0000
15	0.0	0.0	0.0	131.	0	0.0	0.0	0	0	C-0	0	0.0000
16	0.0	0.0	0.0	131.	0	0.0	0.0	0	0	C-0	0	0.0000
17	0.0	0.0	0.0	131.	0	0.0	0.0	0	0	C-0	0	0.0000
18	0.0	0.0	0.0	131.	0	0.0	0.0	0	0	C-0	0	0.0000
19	0.0	0.0	0.0	131.	0	0.0	0.0	0	0	C-0	0	0.0000
20	0.0	0.0	0.0	131.	0	0.0	0.0	0	0	C-0	0	0.0000
21	4.4	4.4	0.0	131.	0	3.5	0.0	1	368.	C-0	0	0.0000
22	5.5	5.5	0.0	131.	0	4.4	0.0	1	914.	C-0	0	23.5 201.
23	11.4	11.4	0.0	131.	4	2652.	10.1	1	1372.	C-0	0	35.2 143.
24	19.0	19.4	0.0	131.	9	2205.	12.0	0	1073.	C-0	0	66.4 107.
25	22.9	22.4	0.0	131.	15	1456.	10.1	0	1345.	C-0	0	64.9 229.
26	27.3	27.4	0.0	131.	21	1567.	17.8	0	907.	C-0	0	66.4 143.
27	27.5	27.2	0.0	131.	27	2722.	3.9	0	1087.	C-0	0	35.4 245.
28	27.8	27.0	0.0	131.	32	575.	6.2	0	1115.	C-0	0	46.9 154.
29	31.7	31.5	-1.5	131.	37	1017.	10.9	0	1219.	C-0	0	65.4 206.
30	34.9	34.8	0.0	131.	37	882.	10.4	0	1320.	C-0	0	65.9 173.
31	36.6	36.4	0.0	132.	42	782.	16.0	0	1407.	C-0	0	67.3 180.
32	36.0	36.3	0.0	132.	45	115.	3.9	0	1454.	C-0	0	36.0 96.
33	36.4	36.4	0.0	132.	44	-353.	-1.6	0	1442.	C-0	0	37.0 96.
34	36.4	36.4	0.0	132.	47	-346.	-1.7	0	1404.	C-0	0	36.4 0.
35	36.4	36.4	0.0	132.	40	-36.8	-1.7	0	1165.	C-0	0	36.4 0.
36	36.7	36.7	0.0	132.	36	-307.	-1.4	0	1110.	C-0	0	37.1 0.
37	36.0	36.3	0.0	132.	36	-36.6.	-1.6	0	1714.	C-0	0	37.1 0.
38	36.4	36.4	0.0	132.	36	-1717.	-11.9	0	1165.	C-0	0	36.4 0.
39	36.4	36.4	0.0	131.	22	-4270.	-7.5	0	1027.	C-0	0	36.4 0.
40	36.4	36.4	0.0	131.	20	123.	2.0	0	966.	C-0	0	24.2 0.
41	36.4	36.5	0.0	131.	20	115.	2.0	0	976.	C-0	0	24.2 91.
42	36.7	36.7	0.0	131.	21	106.	2.0	0	990.	C-0	0	24.2 47.
43	36.4	36.4	0.0	131.	22	391.	4.1	0	1016.	C-0	0	35.4 131.
44	36.4	36.4	0.0	131.	24	660.	6.5	0	1071.	C-0	0	41.6 162.
45	36.4	36.4	0.0	132.	29	1151.	11.4	0	1165.	C-0	0	65.4 214.
46	36.4	36.4	0.0	132.	35	944.	10.6	0	1276.	C-0	0	61.7 196.
47	36.4	36.4	0.0	132.	40	821.	10.1	0	1369.	C-0	0	61.1 187.
48	36.4	36.4	0.0	132.	45	716.	9.6	0	1451.	C-0	0	67.5 179.
49	36.4	36.4	0.0	132.	46	-261.	-7	0	1475.	C-0	0	60.0 0.
50	36.4	36.2	0.0	132.	45	-69.	1.3	0	1458.	C-0	0	64.2 65.
51	36.4	36.1	0.0	132.	42	-790.	-5.6	0	1413.	C-0	0	45.5 0.

Fig. 12.- (cont.)

TIME (sec)	VOLTAGE (mV/mA)	WELL-CUT EXPIRATION	DEVIATION (mV/mA)	F-BULL (mV)	F-AIR (mV)	F-AIR (mV)	INPUT-POWER (mV)	SHFT-PWM (mV/mA)	CGNTRLLR SELECT (mV/mA)	MTR VOLTS	AMP AMPS	BAT DISCHARGE (2)
241	91.8	79.5	-11.9	145.	213.	177.	5.5	6.0	3 3165. 6171.	5	65.9	90.
242	90.5	79.2	-11.6	146.	214.	177.	5.5	6.1	3 3178. 6176.	5	69.7	70.
243	90.4	79.5	-11.0	146.	216.	115.	5.5	6.0	3 3190. 6221.	5	65.9	69.
244	90.5	79.8	-10.7	146.	218.	115.	5.5	6.0	3 3202. 6244.	5	65.9	69.
245	90.4	80.1	-10.4	146.	217.	115.	5.5	6.2	3 3214. 6268.	5	65.9	69.
246	90.4	80.1	-10.1	146.	221.	107.	5.4	6.1	3 3226. 6279.	5	65.9	69.
247	90.5	80.7	-5.6	146.	222.	107.	5.4	6.2	3 3237. 6312.	5	7C.0	88.
248	90.4	80.9	-9.1	146.	224.	100.	5.4	6.1	3 3248. 6334.	5	7C.0	88.
249	89.9	81.2	-6.7	147.	225.	99.	5.4	6.2	3 3258. 6354.	5	7C.0	88.
250	89.4	81.5	-7.9	147.	227.	99.	5.4	6.3	3 3279. 6374.	5	7C.0	88.
251	89.2	81.7	-6.6	147.	228.	91.	5.4	6.2	3 3279. 6394.	5	7C.0	87.
252	87.4	81.9	-5.5	147.	230.	92.	5.4	6.3	3 3288. 6413.	5	7C.0	87.
253	86.6	82.1	-4.7	147.	231.	84.	5.4	6.2	3 3298. 6430.	5	7C.0	87.
254	86.4	82.4	-6.1	147.	232.	84.	5.4	6.3	3 3307. 6448.	5	7C.0	86.
255	86.6	82.6	-5.4	147.	233.	84.	5.4	6.3	3 3315. 6465.	5	7C.0	86.
256	86.9	82.8	-7.6	146.	235.	77.	5.4	6.2	3 3324. 6481.	5	7C.0	87.
257	86.3	83.0	-7.4	148.	236.	77.	5.4	6.3	3 3332. 6497.	5	7C.0	86.
258	86.5	83.2	-7.3	148.	237.	77.	5.4	6.4	3 3340. 6513.	5	7C.1	66.
259	83.4	83.4	-7.5	146.	238.	77.	5.4	6.4	3 3348. 6526.	5	7C.1	65.
260	86.7	81.6	-7.1	146.	239.	69.	5.4	6.3	3 3356. 6547.	5	7C.1	65.
261	86.7	81.6	-7.1	146.	240.	69.	5.4	6.4	3 3356. 6557.	5	7C.1	65.
262	85.7	80.7	-2.4	146.	235.	77.	5.4	6.4	3 3370. 6571.	5	7C.1	65.
263	85.4	80.7	-1.6	148.	241.	69.	5.4	6.4	3 3372. 6585.	5	7C.1	65.
264	84.4	80.8	-0.8	148.	242.	61.	5.4	6.3	3 3383. 6597.	5	7C.1	65.
265	84.2	80.2	-0.6	148.	243.	61.	5.4	6.2	3 3393. 6603.	5	7C.1	65.
266	80.4	80.4	-0.0	149.	242.	-307.	2.5	0.0	3 3370. 6522.	4	48.0	58.
267	81.7	81.7	-0.3	148.	239.	69.	5.3	6.3	3 3356. 6547.	5	7C.1	65.
268	81.2	81.7	-0.5	146.	239.	69.	5.3	6.3	3 3356. 6548.	5	7C.1	65.
269	85.4	83.9	-1.6	148.	241.	69.	5.4	6.4	3 3355. 6552.	5	7C.1	65.
270	84.4	84.2	-0.8	148.	242.	61.	5.4	6.3	3 3345. 6527.	5	7C.1	65.
271	82.5	82.5	0.0	147.	243.	61.	5.4	6.3	3 3366. 6595.	5	7C.1	66.
272	82.7	82.7	0.0	147.	234.	-121.	5.4	1.4	3 3313. 6516.	5	7C.1	66.
273	82.3	82.9	-1.1	147.	244.	61.	5.4	6.3	3 3323. 6479.	5	7C.1	66.
274	82.3	82.3	0.0	147.	219.	-122.	5.4	1.6	3 3327. 6472.	5	7C.0	66.
275	82.6	82.6	0.0	148.	216.	-61.	5.4	6.3	3 3355. 6542.	5	7C.1	65.
276	81.4	81.4	-2.4	146.	236.	-123.	5.4	1.4	3 3345. 6527.	5	7C.1	65.
277	82.5	82.5	0.0	147.	234.	-121.	5.4	1.4	3 3363. 6595.	5	7C.1	66.
278	82.7	82.7	-2.7	147.	214.	61.	5.4	6.3	3 3323. 6479.	5	7C.1	66.
279	82.1	82.1	-1.4	146.	215.	77.	5.4	6.3	3 3327. 6487.	5	7C.0	66.
280	82.4	82.4	-1.7	148.	217.	77.	5.4	6.3	3 3343. 6519.	5	7C.1	66.
281	82.5	82.5	0.0	147.	218.	70.	5.4	6.3	3 3351. 6534.	5	7C.1	66.
282	85.7	85.7	-2.6	147.	237.	69.	5.4	6.4	3 3358. 6548.	5	7C.1	66.
283	86.5	86.5	-2.7	146.	240.	69.	5.4	6.3	3 3370. 6473.	5	7C.0	66.
284	87.3	87.3	-2.4	147.	215.	77.	5.4	6.3	3 3327. 6487.	5	7C.0	66.
285	87.4	87.4	-2.4	147.	216.	77.	5.4	6.3	3 3343. 6519.	5	7C.1	66.
286	87.5	87.5	-2.7	147.	217.	70.	5.4	6.4	3 3351. 6534.	5	7C.1	66.
287	84.1	84.1	-2.4	147.	244.	62.	5.4	6.4	3 3370. 6473.	5	7C.1	66.
288	87.7	87.7	-2.7	147.	245.	61.	5.4	6.4	3 3370. 6473.	5	7C.1	66.
289	87.9	87.9	-2.4	147.	246.	-415.	2.2	0.0	3 3307. 6635.	0	C.0	0.
290	82.5	82.5	0.0	147.	234.	-214.	0.0	0.0	3 3349. 6630.	5	7C.0	66.
291	82.4	82.4	-0.2	147.	234.	0.	0.0	0.0	3 3316. 6467.	5	7C.0	66.
292	81.9	81.9	-0.2	147.	232.	-169.	5.3	0.1	3 3307. 6450.	5	7C.0	66.

Fig 12--(cont.)

TIPF ESE)	VELO-SCH EHP/PRI	VELO-ACT EHP/PRI	DEVIATION EHP/PRI	F-ROLL (INT)	F-AIR (INT)	F-ACCEL (INT)	F-ALR (INT)	INPUT-POWER (MTP) (HYD)	GEAR SELECT (INT)(HYD)	SHAFT-RPM STEP/FIELD	CONTROLLER VOLTS	MTR AMPS	BAT DISCHARGE 121	
1115	0.0	0.0	0.0	0.0	0.0	0.0	0.0	0.0	0.0	0.0	0.0	0.0	0.0	
1116	C.C	0.0	C.0	C.0	0.0	0.0	0.0	0.0	0.0	1	0.0	0.0	122-P125	
1117	C.C	0.0	C.0	C.0	0.0	0.0	0.0	0.0	0.0	0.0	0.0	0.0	122-P127	
1118	2.4	3.0	0.0	0.0	0.0	0.0	0.0	0.0	0.0	0.0	0.0	0.0	122-P128	
1119	7.7	6.1	-0.9	0.0	1911.	1.1	0.0	1	201*	1	11.0	152*	122-P134	
1120	11.0	12.3	-5.5	0.0	2770.	5.3	0.0	1	695.	3	35.0	160*	122-P135	
1141	1P-1	10.9	-4.6	4.0	2940.	10.5	0.0	1	1297.	5	66.0	196*	122-P136	
1142	21.1	2C.7	-1.4	0.0	2372.	12.0	0.0	2	1055.	5	65.0	233*	122-P137	
1143	24.2	27.6	-1.7	0.0	780.	5.6	0.0	2	1100.	4	4t.4	138*	122-P138	
1144	24.9	32.6	-7.7	0.0	1280.	2.0	0.0	2	1461.	5	65.7	179*	122-P139	
1145	29.1	29.1	-7.7	0.0	1401.	12.4	0.0	1	1012.	5	64.0	237*	122-P140	
1146	31.2	31.2	-11.8	0.0	280.	5.6	0.0	1	1140.	4	4t.1	154*	122-P141	
1147	32.6	32.6	-6.0	0.0	327.	10.9	0.0	3	1224.	5	65.6	206*	122-P142	
1148	34.1	32.2	-1.2	0.0	35.	1P5.	0.0	3	12n9.	5	3x.7	107*	122-P143	
1149	34.1	34.6	-1.4	0.0	387.	8.6	0.0	3	1144.	5	6t.2	191.	122-P144	
1150	35.2	35.2	-1.2	0.0	41.	1.1	0.0	3	1346.	5	3t.0	100*	122-P145	
1151	35.2	35.2	-1.2	0.0	42.	123.	1.3	0.0	1409.	3	3t.0	99.	122-P146	
1152	36.5	36.5	-1.2	0.0	112.	4.6	1.4	0.0	1432.	4	4t.6	127.	122-P147	
1153	36.5	36.5	-1.2	0.0	45.	-107.	-1.1	0.0	1411.	0	C.0	0.	122-P148	
1154	37.9	37.9	-1.2	0.0	47.	-246.	-0.6	0.0	1404.	0	C.0	0.	122-P149	
1155	37.9	37.9	-1.2	0.0	50.	-367.	-1.1	0.0	1175.	0	C.0	0.	122-P150	
1156	37.9	37.9	-1.2	0.0	53.	-366.	-1.6	0.0	1319.	0	C.0	0.	122-P151	
1157	31.4	31.4	-1.2	0.0	112.	55.	-107.	-1.1	0.0	1304.	0	C.0	0.	122-P152
1158	26.4	26.4	-1.2	0.0	35.	-246.	-6.4	0.0	1275.	0	C.0	0.	122-P153	
1159	26.4	26.4	-1.2	0.0	37.	-615.	-6.0	0.0	1227.	0	C.0	0.	122-P154	
1160	26.4	26.4	-1.2	0.0	29.	-614.	-1.4	0.0	1159.	0	C.0	0.	122-P155	
1161	26.4	26.4	-1.2	0.0	25.	-614.	-1.4	0.0	1095.	0	C.0	0.	122-P156	
1162	27.4	27.4	-1.2	0.0	21.	-614.	-1.0	0.0	1030.	0	C.0	0.	122-P157	
1163	17.1	17.1	-1.2	0.0	121.	19.	-921.	-4.7	0.0	950.	0	C.0	0.	122-P158
1164	12.6	12.6	-0.0	0.0	111.	14.	-1847.	-8.0	0.0	8C5.	0	C.0	0.	122-P159
1165	8.1	8.1	-0.3	0.0	111.	6.	-1847.	-6.7	0.0	612.	0	C.0	0.	122-P160
1166	4.0	4.0	-0.0	0.0	111.	4.	-1898.	-4.7	0.0	2.	695.	0	C.0	0.
1167	C.C	0.0	C.0	C.0	111.	1.	-2491.	-1.5	0.0	1.	748.	0	C.0	0.
1168	C.C	0.0	C.0	C.0	111.	0.	-2306.	-1.1	0.0	1.	243.	0	C.0	0.
1169	C.C	0.0	C.0	C.0	111.	0.	0.	0.0	0.0	1.	0.	0	C.0	0.
1170	C.C	0.0	C.0	C.0	111.	0.	0.	0.0	0.0	1.	0.	0	C.0	0.
TOTAL CYCLE TIME (INT) = 22.8167														
TOTAL CYCLE DISTANCE (KPS) = 11.6328														
TOTAL PRIOR INPUT ENERGY (KWH-HR) = 1.1754														
PRIOR DISCHARGE AT END OF CYCLE (A2) = 1.1012														
TC1ST FACING INPUT ENERGY (KWH-HR) = 0.1755														
TC1ST REGENERATION ENERGY AVAILABLE (KWH-HR) = 0.1755														
TC1ST FACING ENERGY COST (\$/KWH) = .0000														
TC1ST REGENERATION ENERGY COST (\$/KWH) = .0000														

Fig. 12 (cont.)

Fig 13. Hybrid Vehicle Cruise Simulation

Following successful coding of the models into the program EVSIM, a test bed vehicle was needed to validate the EV simulation. This test vehicle could then be used to investigate innovative concepts to improve EV energy efficiency.

IV. Hardware Implementation of the EV

Construction of a test bed EV was needed as a source of data to validate the simulation EVSIM and to investigate new efficiency and operability concepts for EV's. Since portions of the preliminary design of the test bed vehicle proceeded in parallel with the simulation development, some components selection was based on a preliminary analysis of the desired performance and candidate drive systems.

Candidate Selection

Table III lists the major components of any electric vehicle system and includes the options considered for the test vehicle. In addition to the performance requirements listed in the previous section, this vehicle was also

TABLE III
Electric Vehicle Components

Batteries	Controllers	Motor	Transmissions
Lead-Acid	Battery Switching	DC Shunt	Fixed Ratio
-Std Automotive			
-Industrial	Chopper	DC Series	Gear Ratio
-Golf-cart			
Nickel Zinc			Continuously
Nickel Iron			Variable

constrained to use readily available components and remain flexible enough to incorporate various modifications during follow-on investigation. Many conceivable component options were not included in Table III due to their current lack of commercial availability or apparent lack of suitability for the test vehicle. Alternative current (AC) motors were not considered, for example, due to the control complications and associated losses with the required DC to AC inverters (Reference 16). Similarly, several highly regarded battery types (such as zinc-chlorine hydrate and sodium sulfur), although possessing significantly better potential performance than lead-acid batteries (Reference 14, 22, 32, 35), were not options for the test vehicle due to their present lack of development and availability.

While in general, the interactions between the various basic power train components encourages a systems' viewpoint toward their selection or elimination, certain individual component decisions were made based simply on the constraints of the test-bed vehicle. The reasonable flexibility and the immediate availability of a multi-speed gear ratio transmission made it the obvious design choice. The battery selection also could be reasonably

separated from other component influences. The 21 kwh energy storage and 22 kw peak power demands were both severe restrictions that eliminated certain battery candidates.

With lead-acid batteries, high energy and high power densities cannot be simultaneously optimized within the same design (References 25, 35). Standard automotive starting, lighting and ignition (SLI) batteries, for example, have very high power densities (up to 200 w/kg for starting intervals, Reference 32), but were eliminated from final consideration due to their inability to recover from repeated deep discharges. At the other end of the spectrum are the industrial designs. These are designed for applications such as electric lift trucks, where weight and physical size are not critical considerations and maximum peak power demands are not appreciably above average levels. They can sustain up to 2000 deep cycle discharges that have limiting power densities below 20 w/kg (Reference 32). Golf-cart batteries were developed to provide reasonable power densities (up to 100 w/kg) while maintaining deep-discharge life expectancies of 200 to 400 cycles (References 22, 32); as such, they represent the best lead-acid alternative.

Both high power density and high energy density are potentially attainable with the two nickel-based battery candidates. Unfortunately, recent laboratory and vehicle test of nickel-zinc designs have failed to substantiate their projected performance and have shown especially poor deep-discharge cycle life (Reference 15). The nickel-iron, or "Edison" battery, on the other hand, has demonstrated excellent cycle life (1000+), as well as high power density (130 w/kg) and approximately 25 percent higher energy density than lead-acid batteries. Poor energy efficiency, however, is a strong deterrent against the design. Due largely to excessive hydrogen gas evolution during charging, average charge/discharge efficiency is typically 50 percent which is about one-third lower than that reported for lead-acid batteries. Considering all the reasonable options then, lead-acid golf-cart style batteries were selected as being the most practical and energy efficient.

The choice of a motor and controller was not as clear. Series motors have traditionally been used for traction motors due to their high starting torque characteristic. Shunt motors, on the other hand, offer much better speed regulation and the opportunity, with separate field control, to greatly reduce the current handling requirements of the control circuitry. Either of the proposed controller types can be effective with either motor; however, the over-current sensitivity of the shunt motors at low speeds (Reference 16) strongly encourages the sort of current-limiting circuits as are typically included in solid state chopper controls. In the final analysis, the low speed torque capability of the series motor and the simplicity and flexibility of the battery-switching controller prompted their selection for incorporation into the test-bed vehicle.

Test Vehicle Design

Once the general configuration of lead-acid batteries, battery-switching controller, series motor, and multi-ratio transmission was

selected, the actual component sizing and vehicle designing could proceed. The most obvious physical constraints came directly from the vehicle chassis that was available. The total number of batteries that could be conveniently installed within the body of the car while retaining four passenger capability was twelve. Based on the standard 29 kg, six-volt golf-cart battery, this constraint resulted in a 72 volt, 350 kg battery pack. The net energy capacity of the system at a two-hour discharge rate was calculated by multiplying the energy density of 30 wh/kg (Reference 32) by the battery mass to obtain 10.5 kwh. This realization pointed out the facts that the battery system alone could not provide the 21 kwh necessary for the desired 160 km cruise range, and that the maximum power that could be drawn from the batteries over the two hours was 5.25 kw. This power capacity led to motor power rating of 6 kw. Since series motors can develop up to four times their rated power (References 4, 13) for limited durations, the 22 kw acceleration power requirements was attainable.

The most significant conclusion of the battery energy limitation was that some auxiliary energy source (i.e. hybrid) was required. Two gasoline-powered hybrid arrangements were considered. A series hybrid system was first investigated, but discarded due to its low conversion efficiency of approximately forty percent of mechanical motion to stored battery energy (References 32, 41).

A parallel hybrid system, as indicated in Figure 14 reduces considerably the total losses to the engine/motor coupling inefficiencies. Efficiencies of approximately ninety percent are achievable. This was the system selected for the test vehicle. Since the motor could provide enough power to meet the urban acceleration demands, the prime function of the hybrid engine was simply to augment the electric drive during high speed cruise. Besides supplying the added power required for cruise speed, with appropriate engine/motor ratios, hybrid augmentation could actually reduce the motor current demand, thus extending the battery range. A coupling ratio was thus established that would allow high speed cruise in a relatively low transmission ratio to cause a high motor shaft speed. Increasing the speed of a series motor automatically reduces its current demand.

For the test vehicle, a parallel shaft V-belt drive was designed. V-belt drive had the advantages of high efficiency (~ 96 percent) and speed ratio flexibility through alternate sheave combinations (Reference 20). One sheave was mounted onto the motor shaft such that the hybrid power could be directly coupled to the motor output. A belt-tightener clutching arrangement permitted the hybrid engine to be disconnected during slow-speed pure electric operating modes. The constantly turning motor sheave could then be used to start the hybrid engine when the appropriate vehicle speed was reached. For initial test purposes, the clutching mechanism was designed to be manually operated by the vehicle driver.

Once the preliminary design concepts were established for the test vehicle from use of EVSIM and analysis, the detailed component hardware was designed. Included in this design was a lightweight motor mounting bracket that provides positive shaft alignment as well as a mounting pad for the hybrid engine bracket and one for any future ancillary test equipment. The motor to transmission coupling was designed with an outside taper such that a variety of stock taper-lock V-belt sheaves can be mounted. This coupling

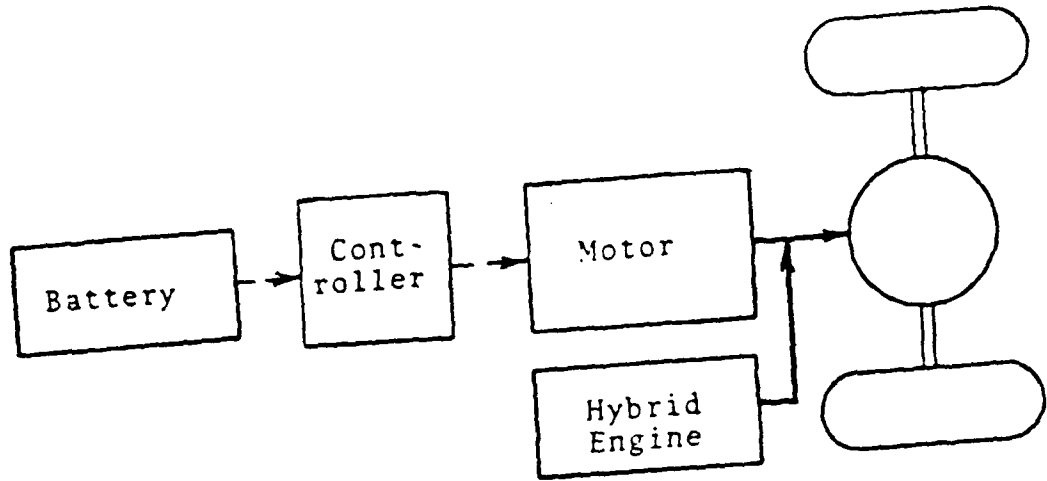


Fig 14 Parallel Hybrid Vehicle Block Diagram

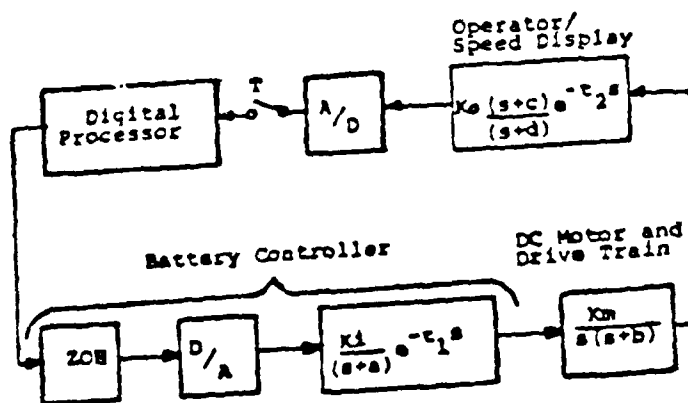


Fig 15 Type I Controller

also incorporates a separate bearing to absorb the V-belt created side loads. A final notable design feature for the baseline test vehicle was the five-step battery-switching controller developed. Using eight high-current diodes and seven relay switches, five voltage ranges, including 12, 24, 36, 48, and 72 volts, are available.

Test Vehicle Baseline Hardware Requirements

The performance requirements for the test-bed vehicle were 90 km/hr top speed, 0 to 50 km/hr in fifteen seconds, two hours urban endurance, and 160 km range at 80 km/hr cruise. The selected baseline system as described by EVSIM in Figure 12 whose urban performance is also indicated in Figure 12, meets these requirements. Note from the input parameter listing in Figure 12 and the portions of the driving cycle displayed that the selected hybrid system operates in a pure electric mode until the gasoline engine engaged at 45 km/hr to improve the high-speed cruise performance. With the system's 6 kw series motor, 7.5 kw gasoline engine and 72 volt, 350 kg lead-acid battery pack, EVSIM predicted a top speed of 90 km/hr (hybrid engine rpm-limited) and zero to 50 km/hr acceleration in 13 seconds. A constant 88 km/hr cruise sequence (Figure 13) indicated a range of 173 km for 100 percent battery discharge with an ending top speed of 86.9 km/hr. The extrapolated urban endurance based on the battery discharge during one 23-minute cycle was two hours and 37 minutes. Average direct operating energy costs predicted were \$.012/km for the urban environment and \$.0188/km for the high-speed cruise sequence. This is based on a cost of \$.35/liter for gasoline and \$.06/kwhr for electricity. This differential can be explained by the higher cost of fuel being consumed by the hybrid engine during cruise as opposed to the nearly pure electric power used in urban operation.

EVSIM's system design mode was also used to develop an all-electric series motor system that would have the equivalent high-speed range and performance of the hybrid design. This configuration required 1200 kg of battery and a 15 kw motor to attain the 160 km range. Additionally, the urban direct operating costs increased to \$.0188/km while the cruise costs marginally decreased to \$.0151/km.

Once a baseline test bed vehicle was designed, it was implemented in hardware. It was instrumented to monitor energy used (instantaneous voltage and current, and accumulated watts used) speed, electric motor rpm, and internal combustion engine (hybrid) rpm. With this instrumentation, the driving cycles used in EVSIM could be easily validated.

Validation

The EVSIM simulation was validated from primarily two sources; the test bed vehicle and available data (References 1, 9, 31, 32, 34). The available data accumulated by DOE and NASA was useful in verifying and validating certain subsystem models such as the vehicle retarding forces and the energy available from the batteries. The test bed vehicle was used to validate the synergistic effect of all models in EVSIM. After a total of over fifty hours of testing the EV in the all electric and hybrid models in both urban and cruise speed schedules, the EVSIM program was found to be within ten percent

of test bed empirical data in all parameter values. Additional tests were conducted on subsystems such as batteries in static tests to validate portions of submodels.

V. Additional Concept Investigation

The baseline test bed vehicle was modified to investigate various controller schemes and control laws as well as battery charging options and vehicle safety operation.

Control Schemes

While the energy storage devices (batteries) are the recognized foremost deficiency for EV's, the power conditioner/controller seems a logical choice to investigate improvements in both performance (drivability and compatibility with existing traffic flow) and efficiency (range).

The three controllers investigated are representative of the types of controllers in use today or proposed for EV's. Type 1 controller is an electro-mechanical three state (discrete energy level) contactor controller. It is simple and reliable in its operational routine. Figure 15 shows a simplified block diagram of this controller with a microcomputer inserted in the loop. Type 2 controller is a six state device which has a number of both power electronics and electro-mechanical components. While this type of controller obviously adds performance flexibility, it is at the cost of operational complexity. The type 3 controller is an effectively continuous (infinite number of states) controller which is primarily power electronics in its component configuration. The type controller is implemented with 256 states when the microcomputer is inserted in the loop.

All of these controllers were first individually configured in a manual mode (driver operated) with mechanical linkages and discrete electronics providing actual inputs for the manual driving tests. The controllers were also individually fitted with interface for a microcomputer so that it could be installed in the control loop of each type. It was then possible supply inputs to the controllers from the processor through appropriate analog interfaces. For the automated driving tests, the vehicle operator would demand a velocity and the processor would interpret this input and convert it to appropriate controller commands for each type controller. These controllers were modeled and their characteristics incorporated into EVSIM.

Microcomputer

The availability of computationally powerful and fast single board microprocessors make them the logical device to implement the control schemes. A Z80 based system was selected (Reference 17). The Z80 is a bus oriented system requiring minimum additional control logic for addressing and reset, as indicated in Figure 16. A Z80 microcomputer also uses a single phase two megahertz system clock to synchronize its operation and a single five volt DC power supply. The serial input/output controller (SIO) has two independently programmable data communication channels. These channels are used to drive the RS-232 interfaces for the operators terminal and the software development computer. The Z80 counter timer circuit (CTC) contains four independently programmable channels, two of which are used as baud rate clocks for the

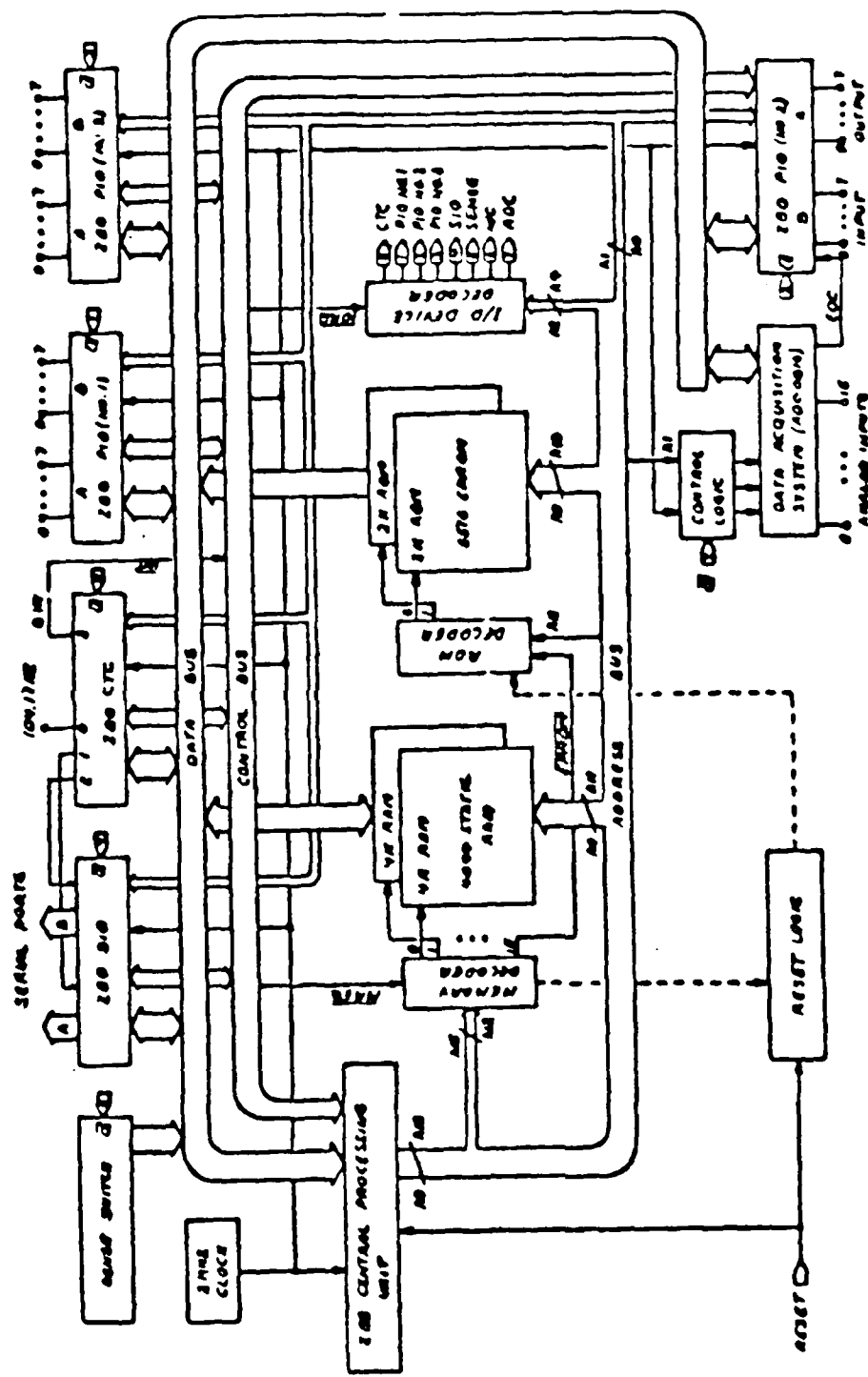


Fig 16 Microcomputer Block Diagram

serial ports of the SIO. The two remaining counter timer channels were cascaded to produce a 104 Hertz low frequency clock and a eight Hertz clock for the control system time reference. Sample period is used to generate interrupt service requests eight times a second and is used by the control software. The microcomputer uses three parallel input/output controllers (PIO) giving a total of six 8-bit parallel data ports for use as input or output interfaces. Each PIO port is independently programmable and is TTL-compatible. When used as an output port, the PIO holds its most recent output state providing the hold mechanism for control interfaces. The microcomputer also employs an analog data acquisition system as an integral part of its design to enhance system flexibility. The analog data acquisition system provides the common functions associated with the collection of analog measurements. It also uses a one Megahertz clock to operate its analog to digital converter and is designed to be interfaced with most microprocessors. The microcomputer uses two types of memory EPROM and RAM. The EPROM is used to store the system monitor, application programs, and provides a means of correcting software errors quickly. A single power supply (+5V) EPROM was selected to minimize power source requirements. RAM memory is used for scratch-pad storage and calculations. The RAM is also used during the software development process to hold new programs for testing and debugging. The low power Schottky TTL components provide the address decoding for the computer memory and input/output devices. The also buffer the Z80 central processing unit and are use in the reset logic that initializes the microcomputer. The control system design has digital interfaces which translate TTL logic level signals into voltage and current signals to direct the power electronics in the high power portion of the controller. These interfaces also provide the power supply, signal ground, and chassis ground isolation for the analog data acquisition system by using optical isolators.

The microcomputer was installed in a research and development mode as shown in Figure 17. Software development was accomplished quickly and efficiently in a second more sophisticated microcomputer. Upon verification, the software was programmed into EPROM's which were subsequently installed into the microcomputer controller. The software flow is shown in Figure 18. The control system had two software programs stored in EPROM's. The first program was the standard "ROM Monitor" operating system for the microcomputer. The second program was application software which implemented the control and energy monitoring functions of the control system. The control functions regulated the vehicle and engine speed. The monitoring function kept a running value of battery energy consumed during a driving cycle. Because of the need for positive regulation of the control system by the operator a "foreground and background" program execution strategy was used. The monitor operating system cycled in the "foreground" waiting for either an operator input or a sample period interrupt. The application program was executed in the "background" on every interrupt cycle to update control and monitoring tasks. The monitor also contained application program commands to initiate the driving cycle and report energy consumption to the operator.

Controller Implementation and Results

To test the various types of controllers, three techniques were used as follows: (a) a digital computer simulation (b) a vehicle test without

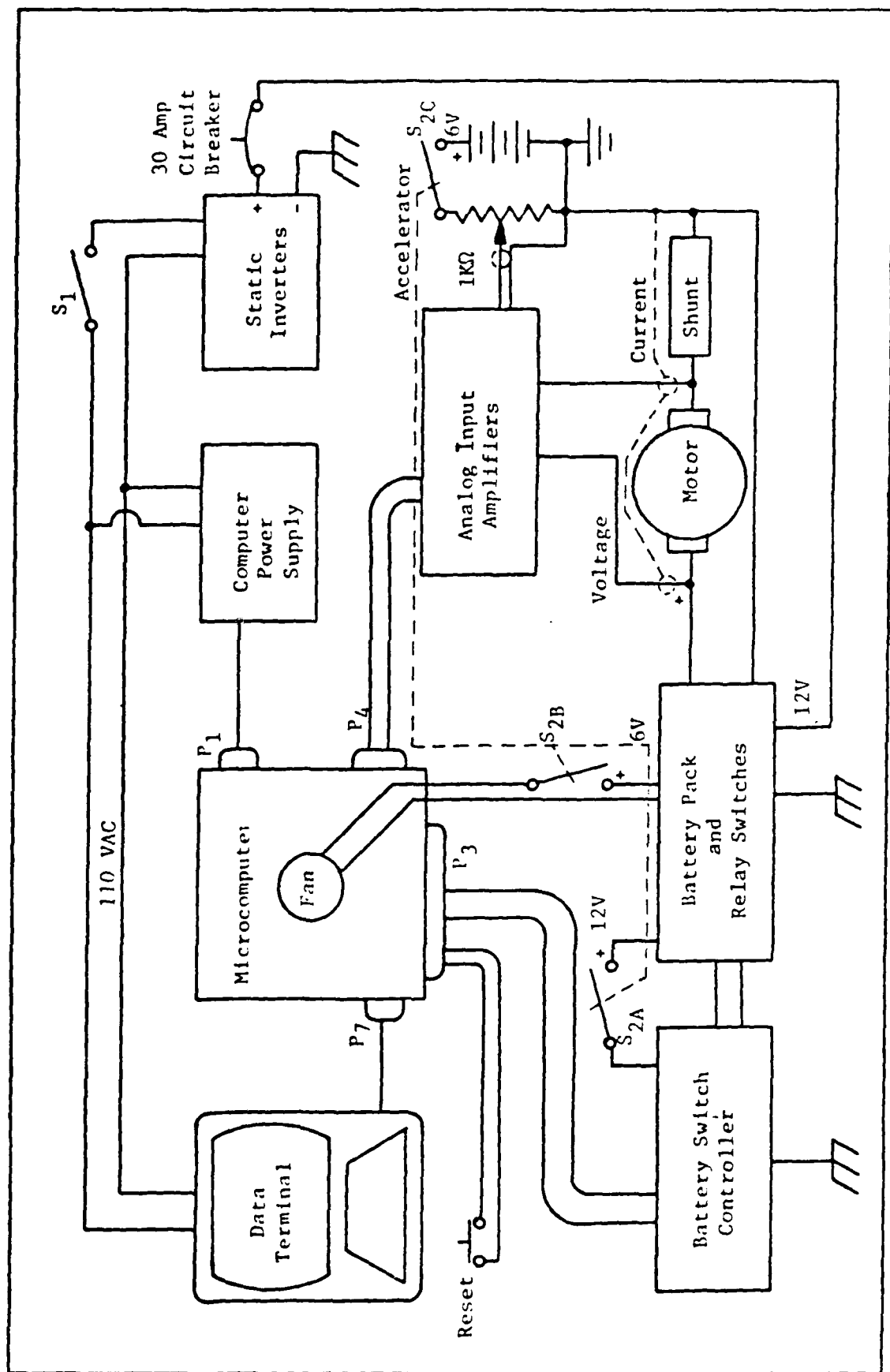


Fig. 17 Electric Vehicle Control System, Test Vehicle Installation

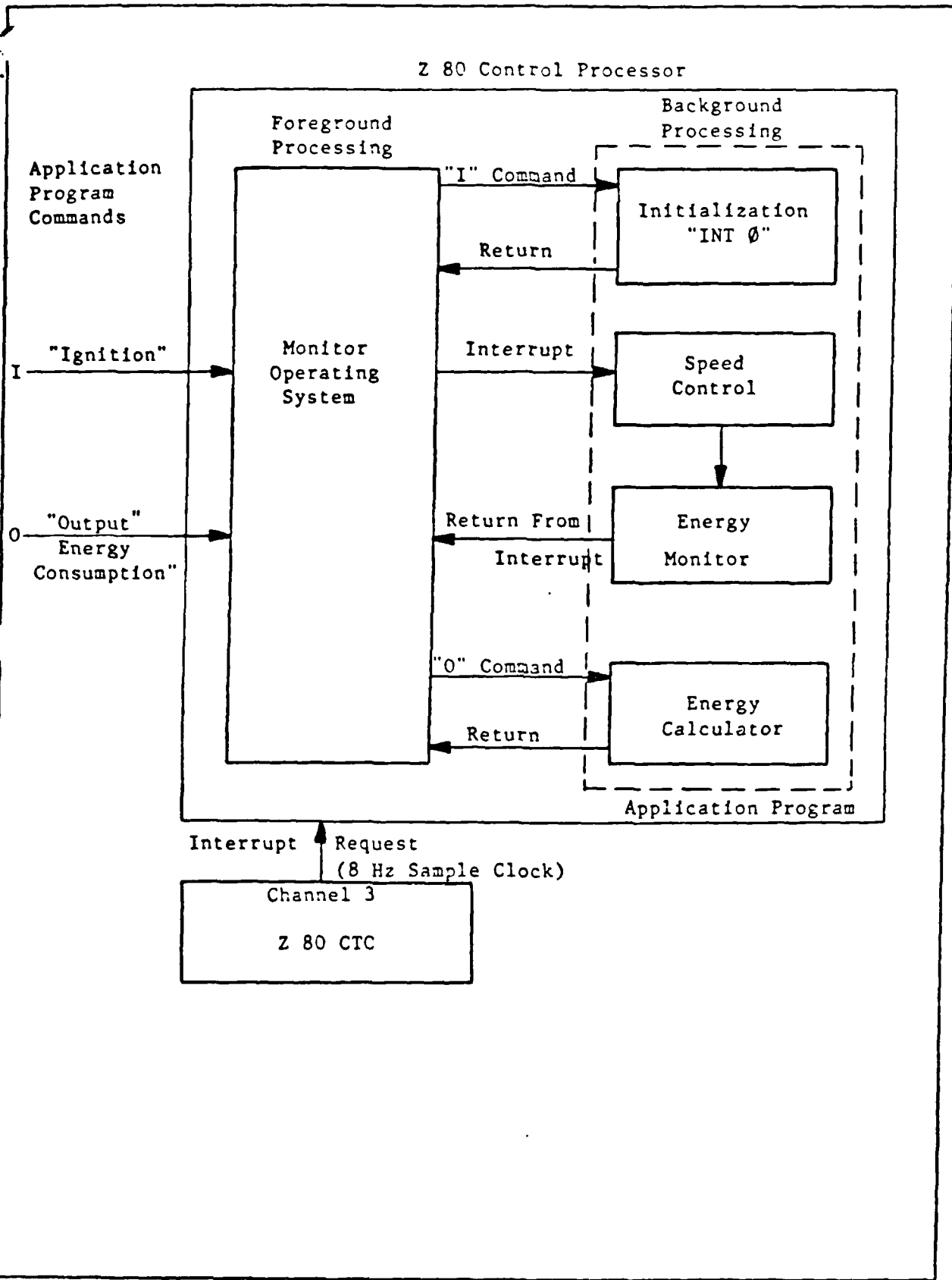


Fig. 18 Software Flow Diagram for the Control System

microcomputer control (c) a vehicle test with microcomputer control.

The controller schemes discussed above were implemented first in EVSIM to test the feasibility of each type. Both the urban driving cycle FUDS (Reference 10) and a constant speed cruise segment (88 km/hr) were simulated for each type.

The test bed vehicle was modified for the road test. The vehicle was configured with the eight bit single board microcomputer described above. Two sets of tests were run for all the controller types. In the first set, all the controllers were manually operator controlled, and in the second set of tests, the controllers were managed by the microcomputer. In the manual tests, the microcomputer was used only to perform some safety functions and the energy monitoring. In the automated tests, the microcomputer was used in the control loop to provide velocity feedback and filter the system control commands by a set of acceleration limits. The microcomputer used stored data and a subsequent table look up to implement type 1 and 2 control laws, and solved an equation to implement the type 3 control law. The vehicle tests were conducted for both urban and cruise segments.

The results of these runs are summarized in Table IV. The energy used and efficiency data was converted to an efficiency measure, percent of range (km) change which is a significant factor for EV's. The digital simulations indicated that a digital computer was compatible with all controller types, and that the efficiency measure increased as expected with the number of control states per controller for all

TABLE IV
Simulation/Vehicle Test Results

	<u>Efficiency Measure (% Range Change)</u>	Speed Schedule	
	Urban (FUDS)	Cruise	Variation (FUDS) (σ , km/hr)
A-D	0	0	9
A-E	7	-3	6
A-F	10	-2	4
B-D	4	2	7
B-E	10	1	4
B-F	13	2	2
C-D	7	6	6
C-E	14	7	3
C-F	19	8	1

A = Manual Operator Control

B = Microcomputer Control

C = Simulation

D = 3 State Controller (type 1)

E = 6 State Controller (type 2)

F = 256 State Controller (type 3)

simulated driving regimes. The microcomputer based controllers showed efficiency measure increases of up to five percent range (two km) over the corresponding manual controllers for the urban driving tests. The data shows that as the number of control states gets large, there is a rapidly decreasing marginal increase in range. The microcomputer based controllers all showed a consistent two km/hr reduction over the manual controllers in speed schedule variation which translates to better traffic flow blending for the EV. All the urban driving tests verified the expected result that the range increased directly with the number of controller states. The cruise segment vehicle tests show that the kind of controller has more effect on range than the number of states for the controller. The maximum increase in range due to the microcomputer controllers in the cruise driving tests was two km. The speed schedule variations for the cruise segment were numerically insignificant. Additionally, results indicated that the speed and precision provided by the microcomputer would increase the efficiency measure for all controller types compared to manual operation for all driving regimes.

These results show that currently available EV electro-mechanical and power electronics configured controllers can be successfully managed by a single-board microcomputer. While these microprocessor based controllers increased the efficiency (range) of the EV tested, these increases were not of the magnitude expected. Besides managing the controllers, the microcomputer's presence in the EV was found to be very convenient and useful as it is in a growing number of conventional petroleum fueled vehicles. The microcomputer performed safety functions such as monitoring the EV systems, checking for malfunctions, and served as a practical way to monitor energy usage. This energy monitoring provided an accurate state-of-charge indicator for the EV. The microcomputer could then act as a manager for battery charging as well as normal discharging which will provide for improved battery operational performance and long battery life.

Optimal Control Law

Because of the improvement made by the multi-state controller (type 3) just discussed, it was logical to investigate whether an optimal control law applied to this plant would produce significant results in terms of both efficiency (minimize energy used) and performance (minimize deviation from demanded speed). The first improvement results directly in more range, and the latter improvement results in increased acceleration performance or drivability.

Optimal Control Design

The optimal control based controller developed in this effort was of low order to match the reduced order model of the EV used. The reduced order model shown in Figure 19 was appropriate for this effort since its accuracy has been shown to be high, and the purpose of the optimal control law investigation was to see if the magnitude of the potential for improved efficiency and performance justifies further pursuit.

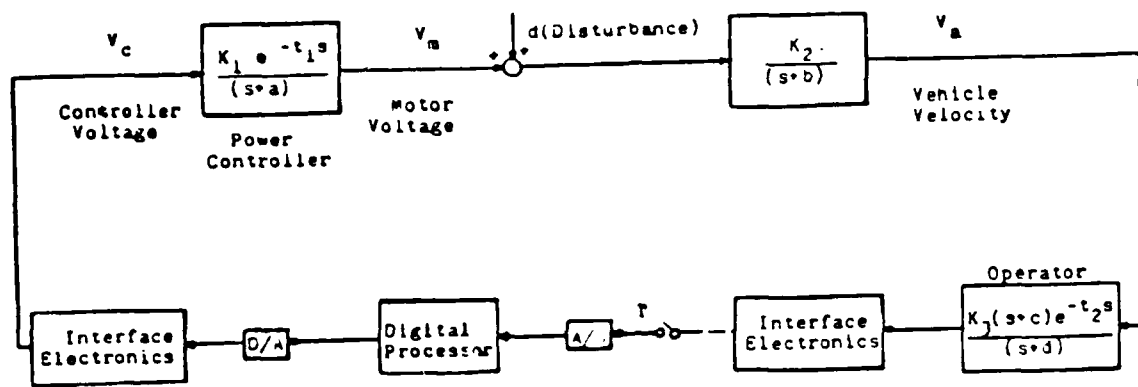


Fig 19 Electric Vehicle System

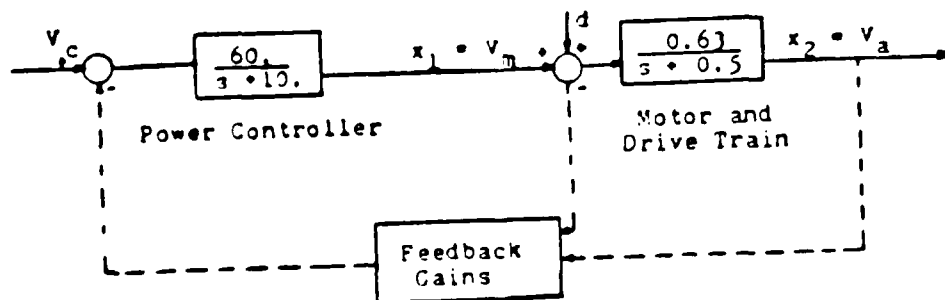


Fig 20 Simplified EV System

The dynamics of the EV system shown in Figure 19 allow several further simplifications. The speed of the digital processor and associated electronics make their effects negligible when compared to the drive train component responses. Similarly, the time delay (t_1) is negligible compared to the dynamics of the other components in the power controller. Since an automated controller is sought, a set point controller seems a logical choice. This controller would tend to minimize the effects of disturbances (wind, road grade and roughness, etc.) and still allow an operator interaction to vary the set point for speed schedule changes and safety considerations. The resulting simplified set point controller is shown in Figure 20. The resulting reduced order state space model is as follows:

$$\dot{\underline{x}} = A \underline{x} + b u + g d \quad (60)$$

$$\begin{aligned} \dot{\underline{x}}_1 &= \begin{bmatrix} -10 & 0 \\ 0.63 - .5 & \end{bmatrix} \begin{bmatrix} \underline{x}_1 \\ \underline{x}_2 \end{bmatrix} + \begin{bmatrix} 60.0 \\ 0 \end{bmatrix} u + \begin{bmatrix} 0 \\ 0.63 \end{bmatrix} d \\ \dot{\underline{x}}_2 & \end{aligned} \quad (61)$$

and

$$Y = C^T \underline{x} = \begin{bmatrix} 0 & 1 \end{bmatrix} \underline{x} = v_a \quad (62)$$

where \underline{x}_1 is the motor voltage, v_a , \underline{x}_2 is the vehicle velocity, v_a , d is the disturbance, and the input u is the controller voltage, v_c . The time response of this system with no feedback for a unit step input for v_c and zero disturbance is shown in Figure 21. As can be seen, the system has a stable overdamped response which illuminates the performance shortfalls of this type of vehicle.

For this set point controller, the quadratic performance index is as follows:

$$J = \frac{1}{2} \int (\underline{x} - \underline{x}_s)^T Q (\underline{x} - \underline{x}_s) + r (v_c - v_{cs})^2 dt \quad (63)$$

where v_c is the set point controller voltage required by the system to reach \underline{x}_s in steady state, $\underline{x}_s = [x_{1s}, x_{2s}]^T$; x_{1s} is the motor voltage at set point velocity; x_{2s} is the set point velocity determined by the operator or speed schedule, J is the cost functional to be minimized; Q is the weighting matrix penalizing deviation from set point state values; and r is the weighting scalar penalizing the use of control. For this linear quadratic set point regulator formulation, an optimal control v_c^* can be found which will minimize the cost functional J . Since both states \underline{x}_1 and \underline{x}_2 are controllable by the input v_c , and both are observable, the problem is properly posed for full state feedback optimal control (Reference 12). The optimal control law which minimizes the cost functional of Equation 63 is:

$$v_c^* = -K^T (\underline{x} - \underline{x}_s) + v_{cs} \quad (64)$$

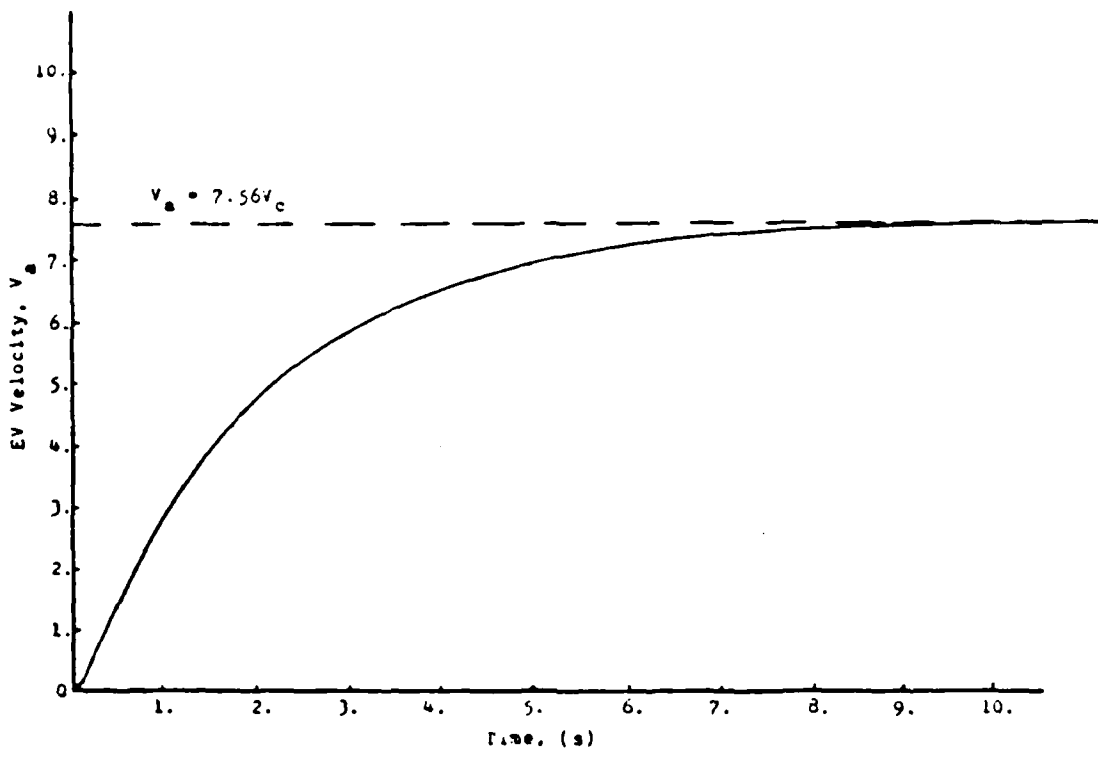


Fig 21 EV Response to Unit Step of Controller Voltage, V_c

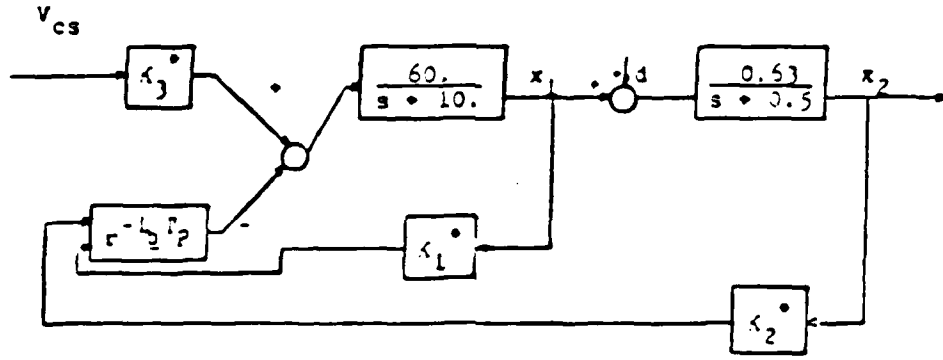


Fig 22 EV Optimal Control Configuration

where

$$\underline{K}^T = (1/r) \underline{b}^T P \quad (65)$$

The matrix P is the steady state Riccati equation solution for the linear quadratic set point problem.

$$A^T P + PA + Q - P \underline{b} \underline{b}^T P \left(\frac{1}{r}\right) = 0 \quad (66)$$

The set point is determined through the scheduled vehicle velocity, v_{as} . That is

$$\underline{x}_s = \begin{bmatrix} x_{1s} \\ x_{2s} \end{bmatrix} = \begin{bmatrix} \frac{\underline{b}}{K_2} v_{as} \\ v_{as} \end{bmatrix} = \begin{bmatrix} 0.8 v_{as} \\ 1.0 v_{as} \end{bmatrix} \quad (67)$$

and

$$v_{cs} = \frac{a}{K_1} \cdot \frac{b}{K_2} v_{as} = 0.13 v_{as} \quad (68)$$

The Q weighting matrix which penalizes state deviation from the set point can be used to tune the optimal controller toward higher performance (quicker response, better drivability). The r scalar (using a single control input) which penalizes the use of control can be used to tune the optimal controller for increased efficiency. As expected with any quadratic performance index, the two objectives of increased performance (through large values in Q) and increased efficiency (through a large value of r) drive the optimal feedback model in opposite directions. Because there is no single combination of Q and r that produces optimal performance for both objectives, several compromise combinations of the weighting elements were investigated. The resulting closed loop system with the optimal feedback gains is shown in Figure 22. The gain K_3^* is used to adjust the final output for correct steady state response.³ Only diagonal elements of the Q matrix were varied

TABLE V
Weighting Parameter Variations

	<u>q₁₁</u>	<u>q₂₂</u>	<u>r</u>
Case 1	1	1	1
Case 2	1	10	1
Case 3	1	100	1
Case 4	1	1000	1
Case 5	1	1	10
Case 6	1	1	100
Case 7	1	1	1000

TABLE VI
Closed Loop Eigenvalues and Feedback Gains

	Eigenvalues	K_1^*	K_2^*	K_3^*
Case 1	-60.82	-0.79	0.852	9.70
Case 2	-60.79	-0.20	0.872	24.70
Case 3	-60.50	-6.26	0.937	75.85
Case 4	-57.11	-20.93	1.125	30.607
Case 5	-21.44	-0.75	0.194	3.22
Case 6	-11.66	-0.60	0.029	1.39
Case 7	-10.18	-0.51	0.003	1.04
Case 8	-5.25	$\pm j3.86$	1.0	8.59

K_3^* assures appropriate steady state response

($Q = \begin{bmatrix} q_{11} & 0 \\ 0 & q_{22} \end{bmatrix}$) because it was evident the q_{22} element corresponding to

state x_2 (velocity) had the main influence on improvements in drivability. Controllers were designed for the set of Q and r elements shown in Table V.

Cases 2 through 4 represent systems optimized for performance and Cases 1 and 5 through 7 represent systems optimized for efficiency. No cases of either $r = 0$, or both q_{11} and $q_{22} = 0$ are included because only physically meaningful and realizable systems were sought (Reference 24). The effective closed loop eigenvalues for the cases are shown in Table II along with the feedback gains. Case 1 for the efficiency oriented systems seems to be a good compromise between speed of response and efficiency achieved. Case 1 was chosen as the efficiency candidate to investigate further. Case 3 was chosen for further investigation from among the performance oriented systems because of its compromise between speed of response and performance in terms of minimized state deviation. Case 8 (Table VI) simulates an operator in the feedback loop modeled as a pure gain ($k = 1$).

Optimal Control System Implementation and Testing

The systems represented by Cases 1, 3, and 8 were implemented in the electric vehicle digital computer simulation EVSIM. The controller subroutine in EVSIM was modified to incorporate the optimal control laws of Cases 1 and 3 as well as the control law for Case 8. Figure 23 shows the comparative system responses to a step change in set point.

A separate look at the various systems responses to disturbances shows Cases 3 and 8 respond about equally well to compensate for road grade and wind disturbances for satisfactory performance. The response of Case 1 to disturbances demonstrates a lack of acceleration performance. Figure 24 shows the relative system responses to a simulated hill.

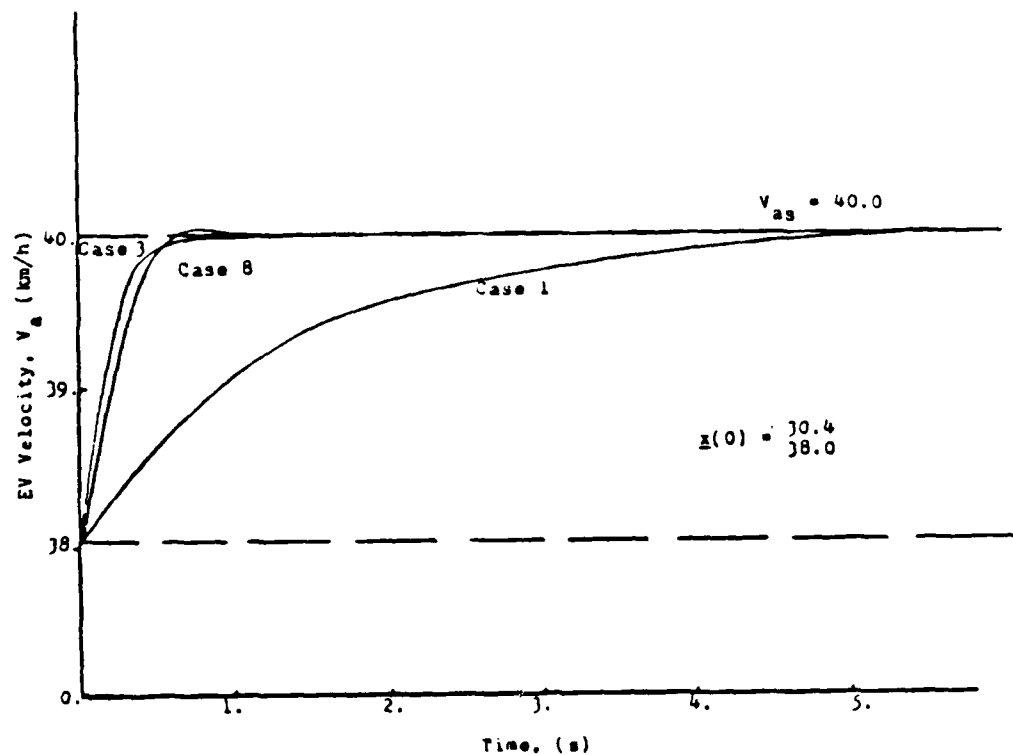


Fig 23 System Response Comparison

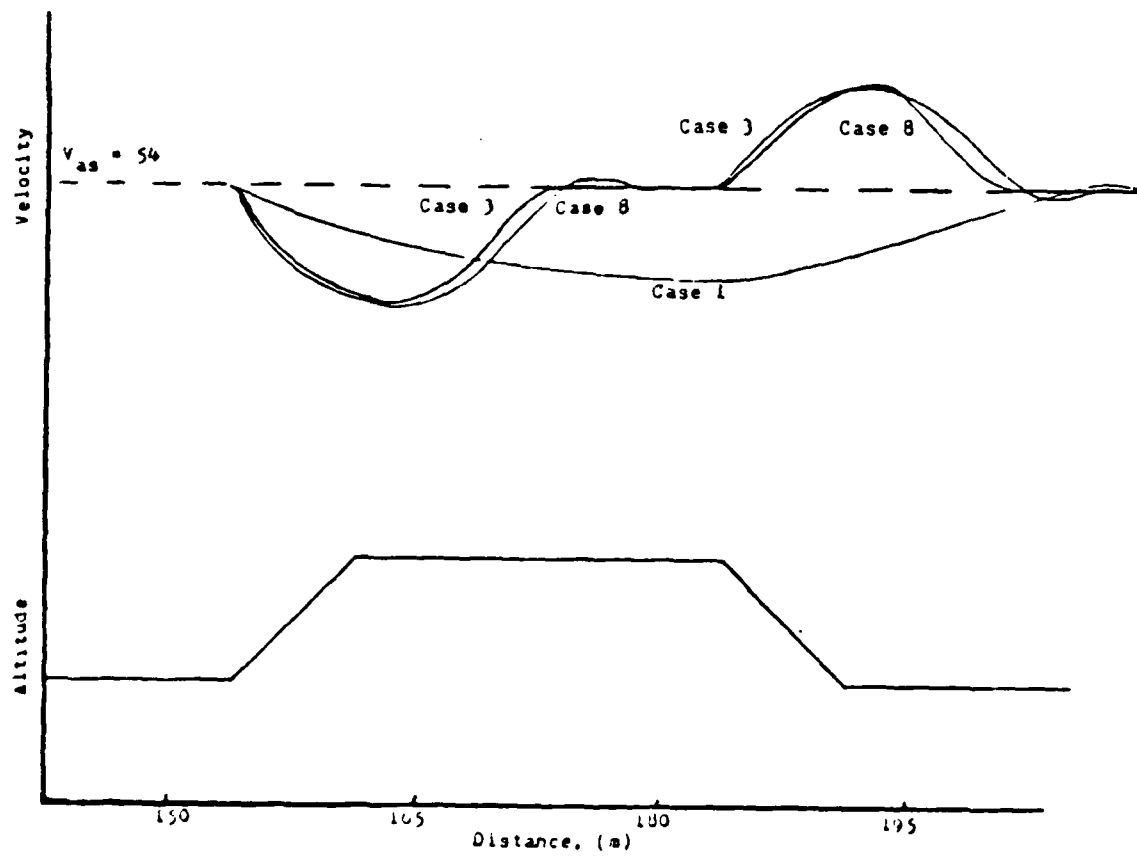


Fig 24 Disturbance Compensation Characteristics

The results of the simulations are displayed in Table VII. Comparing Cases 1 and 3 in the driving segment, it can be seen that Case 1 produces a much more efficient system but at considerable reduction in acceleration performance. Case 3 dominates Case 1 in performance but at a significant cost in efficiency. The relative separation between the two cases is less for the cruise segment but the trends are preserved. The overall performance of Case 8 was surprising in that it came close to matching the drivability of Case 3 and the efficiency of Case 1 for both the driving and cruise segments. Compared to manual controllers, Cases 1 and 8 produced approximately 33 percent increase in range capability while Case 3 produced a 24 percent decrease. The corresponding speed schedule variation was improved by approximately 132 percent for Cases 3 and 8, and decreased by 12 percent by Case 1. Compared to conventional microprocess driven automated controllers, Cases 1 and 8 increased range capability by approximately 11 percent while Case 3 showed a decrease of 35 percent. The corresponding speed schedule variation was improved by approximately 13 percent for Cases 3 and 8 and decreased by 34 percent for Case 1.

TABLE VII

Control System Comparison
Five Minute Driving Segment
(No disturbances)

	Energy Used (kwh)	RMS Speed Schedule Variation (km/h)
Case 1 (Efficiency)	0.91	3.84
Case 3 (Performance)	4.35	1.17
Case 8 (Operator in Loop)	1.06	1.90

Five Minute Cruise Segment
(With disturbances)

Case 1	1.20	2.64
Case 3	3.76	.96
Case 8	1.76	1.28

The results show that optimal control does have a significant effect on EV performance when compared to conventional manual controllers but that no one law was able to produce improvements in both efficiency (range) and performance (drivability). Implementation of the optimal control laws tuned for efficiency (Case 1) and acceleration performance (Case 3) were able to produce 11 and 13 percent improvement respectively in range and speed schedule variation over conventional microprocessor driven automated controllers. While these gains are notable, they are not of the significant magnitude expected.

The performance of microprocessor driven automatic controller with an ideal operator in the feedback loop (Case 8) was surprising that it performed well against all optimal control laws investigated with respect to both efficiency and performance. This would indicate that simple controllers may be able to produce satisfactory results for an EV class of systems, and that as this effort indicates, more complex controllers add only marginal improvements to system operation.

Cases 3 and 8 performed satisfactorily in handling disturbances such as wind and road grade changes, but neither was tuned for this purpose. It is expected that a system specifically tuned to minimize the adverse effects of these disturbances would increase drivability and thereby increase the attractiveness of EV's. Such an area seems potentially attractive for future efforts.

VI. Summary and Conclusions

The electric vehicle simulation program EVSIM does satisfy the primary objective of providing a useful evaluation and design tool for electric vehicle systems. The program has the flexibility to simulate both electric and electric/hybrid configurations using series or shunt motors, step-voltage or continuous controllers, and gear-ratio or continuously variable transmissions for any general shape and size of vehicle. Any specific driving cycle may be used to simulate the vehicle operation. EVSIM has the ability to internally modify a basic input vehicle to provide improved performance to meet required standards.

The general conclusion formed during the validation of EVSIM was that it did indeed provide an easily obtained, accurate evaluation of a vehicle's potential performance. With very little computer time, it clearly illuminated the large and small effects of vehicle component modification. This ability should certainly make the program an efficient tool for both the designer and vehicle evaluator.

Additionally, hybrid power augmentation is required to meet the performance standards set in Chapter II for general purpose USAF passenger cars. The energy available from the state-of-the-art lead-acid batteries is simply insufficient to provide reasonable high-speed cruising range when constrained to the dimensions of a compact vehicle. Until significantly improved batteries become available, a parallel hybrid/electric vehicle is the most feasible alternative to the gas-powered conventional USAF sedan.

It is not clear that the increased efficiency afforded by a microcomputer based controller justifies the microcomputer for EV's. But this increased efficiency capability coupled with a decrease in traffic flow speed variance, and the availability of an accurate energy usage and safety monitor suggest that the microcomputer will make the EV technically and economically feasible for the average urban commuter.

While increases in efficiency and performance can be gained by the application of an optimal control law, these gains were not significant to overcome deficiencies presented by the batteries.

Bibliography

1. AiResearch Manufacturing Company of California. Advanced Electric Propulsion System Concept for Electric Vehicles (Task I Report), (NASA No. 79-15791). Cleveland: NASA Lewis Research Center, 27 April 1979.
2. . Advanced Electric Propulsion System Concept For Electric Vehicles (Task I and II Report), NASA No. 79-16035). Cleveland: NASA Lewis Research Center, 29 June 1979.
3. ASL Engineering Inc. Near-Term Electric Vehicle Program: Phase I. Washington: Energy Research and Development Administration, August 1977.
4. Blalock, Grover C. Direct-Current Machinery. New York: McGraw-Hill Book Co., Inc., 1947.
5. Bose, B.K. and Sutherland, A.H., "A Microcomputer Based Real Time Feedback Controller For An Electric Vehicle Drive System," IEEE Industry Application Society, Conference Record, ISA79: 25F, 1979.
6. Cunningham, Charles E. Chief, Base Support Section, MMME, HQ AFLC. Letter, subject: reply in response to Air Command and Staff College inquiry, to Major Offley, Robins AFB, Ga., 10 November 1977.
7. Davis, D.D., et al. Determinization of the Effectiveness and Feasibility of Regenerative Braking Systems on Electric and Other Automobiles, (NASA No. 78-25440). Livermore, Ca.: California University, 9 September 1977.
8. Department of Energy. DOE Interagency Agreement With the USAF, DE-AIOI-80CS5028. Washington: Government Printing Office, July 1980.
9. . "Electric and Hybrid Vehicle Research, Development, and Demonstration Program: Equivalent Petroleum Based Fuel Economy Calculation," Federal Register, 45(100): 34008-15 (21 May 1980).
10. Department of Transportation. "DHEW Urban Dynamometer Driving Sequency," Federal Register, 35(219): 17288-313 (10 November 1979).
11. DeWispealare, A.R., "Microcomputer Enhanced Energy Efficiency in an Electric Vehicle," IEEE Southeastern Con Proceedings, 82CH1749-1, Destin, FL, 1982.
12. DeWispealare, A.R., "Investigation of Optimal Control For An Electric Vehicle," Proceedings of the IEEE Southeastern Conference, April 1983, pp 587-590.
13. Direct Current Engineering Data. Product information catalog. Fort Smith: Balder Electric Company, September-October 1972.

14. "Electric Cars: Where Batteries Stand," Automotive Industry, 185(13): 81-83 (13 September 1978).
15. "Electric Vehicle Problems," Energy Today, 7(17): 133-34 (29 April 1980).
16. Fitzgerald, A.E., Charles Kingsley, Jr. and Alexander Kisko. Electric Machinery (3rd Edition). New York: McGraw-Hill Book Co., Inc., 1947.
17. Frazier, John C., Electric Vehicle Power Controller, AD Air Force Institute of Technology (ENY), Wright-Patterson AFB OH, December 1981.
18. Founds, David, Research Investigation Results-unpublished, Air Force Institute of Technology, 1982.
19. General Electric Co. Near Term Electric Vehicle Program: Phase I. Washington: Energy Research and Development Administration, August 1977.
20. Heavy Duty V-Belt Drive Design Manual. Product design and information catalog. Denver: The Gates Rubber Company, 1977.
21. Hiroyuki, Imai. "Optimal Acceleration Performance and Storage Battery Voltage of an Electric Automobile Viewed from the Standpoint of the Driving Power Energy," DTIC Technical Report, AD B002005L. Alexandria: Defense Logistics Agency, 1975.
22. Hittman Associates, Inc. Data Base on Batteries, Power Conditioning Equipment, and Photo-Voltaic Arrays, Vol. II. Washington: DOE, Division of Energy Storage Systems, November 1979.
23. Keekauffer, Don. Technical Representative, Chrysler Outboard Corp., Industrial Engines Division, Hartford, CN. Personal correspondence, 2 July 1980.
24. Kirk, D.E., Optimal Control Theory, Prentice-Hall Inc., Englewood Cliffs, New Jersey, 1970.
25. Klunder, Kurt W., and Maurice J Katz. "DOE's Electric Vehicle Battery Program: An Overview," Batteries Today, 8(2): 107-11 (February-March 1980).
26. Kosier, T.D., and W.A. McConnell. "What the Customer Gets," SAE Transactions, 65: 730 (1957).
27. Kusko, Alexander. Solid-State DC Motor Drives. Cambridge: The MIT Press, 1969.
28. Lichty, Lester C. Combustive Engine Processes. New York: McGraw-Hill Book Co., Inc., 1967.
29. Linford, H.B. et al. Power Systems For Electric Vehicles. U.S. Department of Health, Education and Welfare; Cincinnati Ohio, 1967.

30. Lucas, Ted, and Fred Reiss. How to Convert to an Electric Car. New York: Crown Publishers, Inc., 1980.
31. NASA TM-75142. Research on Battery-Operated Electric Road Vehicles. Cleveland: NASA Lewis Research Center, October 1977.
32. NASA TM-73756. State-of-the-Art Assessment of Electric and Hybrid Vehicles. Cleveland: NASA Lewis Research Center, September 1977.
33. Neisler, Troy H. Letter, subject: "Recommendations Resulting from MEEP Project H75-21C, Vehicles, Small Type," to HQ AFLC/LOWCS and HQ USAF/LGTN, 28 June 1977.
34. Offley, Ronald D. Electric Powered On-Base Vehicles. Maxwell AFB, AL: Air Command and Staff College, May 1978.
35. Remirez, Paul. "Battery Development Revs Up, Chemical Engineering, 49: 49-51 (27 August 1979).
36. Renner-Smith, S. "Battery-Saving Flywheel Gives Electric Car Freeway Zip," Popular Science, 215(10): 82-84 (October 1980).
37. Rewlett, B.H., and R. Murray (AiResearch Mfg Co.). Near Term Electric Vehicle Program, Phase I. Washington: Energy Research and Development Administration, August 1977.
38. Shephard, Clarence M. "Design of Primary and Secondary Cells, I. Effect of Polarization and Resistance on Cell Characteristics," Journal of the Electrochemical Society, 112(3): 252-57 (March 1965).
39. . "Design of Primary and Secondary Cells, II. An Equation Describing Battery Discharge," Journal of the Electrochemical Society, 112(7): 657-64 (July 1977).
40. Stafford, K.A., DeWispelare, A.R., "Electric Vehicle Energy User Model" Proceeding of IEEE Southeastern Conference, April 1981.
41. Stafford, Kenneth A., Electric Vehicle Simulation for Design Optimization ADA094734, Air Force Institute of Technology (ENY) Wright-Patterson AFB, OH, December 1980.
42. Taborek, Jaroshav J. Mechanics of Vehicles. Cleveland: Penton Publishing Co., 1957.
43. Vinal, George W. Storage Batteries. New York: John Wiley & Sons, Inc., 1955.
44. Z80-CPU Z80A-CPU Technical Manual, 03-0029-01, Zilog Inc., 1977.
45. 2-Cycle Industrial Engines, 820 Series. Product information sheet. Hartford, CN: Chrysler Outboard Corp., undated.

EVSIM PROGRAM LISTING

```

PROGRAM EVSIM(INPUT,OUTPUT,TAPE5=INPUT,TAPE6=OUTPUT)
DIMENSION V(1400),CR(1C1),CSTP(5),NSTP(10),ETAM(10,30),ETAT(10,20)
C,TSTP(10),REAT(5),RBAT(5),V(1400)
REAL MP,P,PS,KMOT,NSTP,M1,CF,MSH
5 900 FFORMAT(1CF5.2)
901 FCPAT(18F4.1)
PRINT(6,902)
902 FCPAT(1H1,3)E7H+ 0 * ELECTRIC VEHICLE SIMU
CLATION * * *
10 C
C ENTER VEHICLE CONSTANTS. DRAG COEFF(CD),FRONTAL AREA(FA), PAYLOAD
C MASS(MP), FIXED MASS(FM).
C
15 REACD,CD,FA,PP,FM
PRINT(6,903)
903 FCPAT(//20X22HVEHICLE CONSTANTS ARE:)
PRINT(6,9C4)CC,FA,PP,FM
904 FCPAT(35X17HDRAG COEFFICIENT-,F5.2,/35X13HFRONTAL AREA-,F5.2,14H
C(SQUARE METERS,/35X13HPAYLOAD MASS-,F4.0,1CH KILOGRAMS,/35X11HFIXED
20 C MASS-,F4.0)
C
C ENTER ENVIRONMENTAL CONSTANTS. AMBIENT TEMPERATURE(TMP), ELECTRIC
C POWER COST(ECCST), PETROLEUM FUEL COST(FCOST).
C
25 REACT,TMP,ECCST,FCOST
PRINT(6,905)
905 FCPAT(//20X28HENvironmental constants are:)
PRINT(6,9C6)TPP,ECCST,FCOST
906 FCPAT(35X2CHAMBIENT TEMPERATURE-,F4.0,8H CELSIUS,/35X23HELECTRIC
30 CENERGY COST= 1,F4.3,9H PER KWHR,/35X22HPETROLEUM FUEL COST= $,F4.2
C,1CH PER LITEF)
C
C ENTER VEHICLE POWER REDUCTION VARIABLES. ROLLING RADIUS(RR), TIRE
C ROLLING COEFFICIENT(CR), AYLE RATIO(AR), NUMBER OF FORWARD SPEEDS
35 C <0 IF CVT>(IS), MAX VEHICLE DESIGN SPEED(VMAX).
C
REACD,RR,CR,AR,IS,VMAX
PRINT(6,907)
907 FCPAT(//20X30HPOWER REDUCTION VARIABLES ARE:)
PRINT(6,9C8)RR,CR,AR,IS,VMAX
908 FCPAT(35X2CHTIRE ROLLING RADIUS-,F6.3,7H METERS,/35X20HROLLING CO
EFFICIENT-,F7.4,/35X11AXLE RATIO-,F5.2,/35X21HNUMBER FORWARD GEAR
CS-,12,/35X17HMAXIMUM VELOCITY-,F4.0,6H KM/HR)
TFITS.NE.0)10,20
45 10 CONTINUE
C
C ENTER TRANSMISSION RATIOS<IF MULTISPEED>(CR(1S)) ON FIRST CARD. ON
C NEXT CARD ENTER DESIRED MOTOR UPSHIFT AND DOWNSHIFT RPM(UPSHFT,
C DNSHFT).
50 C
REACD,(CR(1S),1=1,IS)
REACD,UPSHFT,DNSHFT
PRINT(6,909)
909 FCPAT(//20X39HFIXED SPEED TRANSMISSION VARIABLES ARE:)
PRINT(6,910)UPSHFT,DNSHFT,CR(1)
910 FCPAT(35X2CHACTOR UPSHIFT SPEED-,F5.0,4H RPM,/35X22HMOTOR DOWNSHE
CFT SPEED-,F5.0,4H RPM,/35X12HGEAR RATIOS-,F6.3)

```

```

      IF (IS.EQ.1)3C,11
11    DC 12 I=2,15
60    12 PRINT(6,911)CR(1)
911   FCRPAT(47X,F6.2)
      GO TO 30
20    CCNTINUE
      C
65 C   ENTER CVT VARIABLES. RATED INPUT POWER(PRATT) AND NUMBER OF SPEED
      C   RATIO STEPS FOR INPUT DATA ON FIRST CARD, EFFICIENCY DATA(ETAT)
      C   ON NEXT CARD SERIES: FIRST CARD- SPEED RATIO STEPS<ITSTP>, FOL-
      C   LOWING CARDS- ETAT<.CT.0 AND .LT.1> IN LOFS.1 FOR EACH % OF PRATT
      C   FROM 5% TO 100%. 2 CARDS REQD FOR EACH TSTP>.
70 C
      READ*,PRATT,[ITSTP
      REAC*,[TSTP(I),I=1,ITSTP]
      DC 21 I=1,ITSTP
      DC 21 J=1,2
75 21  REAC(5,900)(ETAT(I,(J-1)*10+K),K=1,10)
      PRINT(6,912)
912   FCRPAT(/20X49FCNTINUOUSLY VARIABLE TRANSMISSION VARIABLES ARE:)
      PRINT(6,913)PRATT
913   FCRPAT(35X13HPOWER RATING-,F5.1,3H KW)
80 30  CONTINUE
      C
      C   ENTER MOTOR VARIABLES. MOTOR TYPE<PTYP><0=SHUNT,1=SERIES>, K FAC-
      C   TCR(MPOT), ARMATURE RESISTANCE(RARM), FIELD RESISTANCE(RFLD),
      C   RATED POWER(PRATHM), MAX POW. MULTR(IPMAX), MAX CUR(AMAX), BASE SPEED
      C   (BSPD), AND NUMBER OF SPEED STEPS FOR INPUT DATA ON FIRST CARD.
      C   ENTER EFFICIENCY(ETAM) ON NEXT CARD SERIES: FIRST CARD- MOTOR
      C   SPEED RATIO STEPS<RPMP>(<STP>), FOLLOWING CARDS- ETAM<.CT.0 AND
      C   .LT.1> IN LOFS.1 FOR EACH 1% OF PRATHM UP TO 300%<3 CARDS REQD
      C   FCR EACH PSTP>.
90 C
      REAC*,PTYP,MMCT,RARM,RFLD,PRATHM,IPMAX,AMAX,BSPD,IMSTP
      REAC*,[PSTP(I),I=1,IMSTP]
      DC 31 I=1,IMSTP
      DC 31 J=1,3
95 31  REAC(5,900)(ETAM(I,(J-1)*10+K),K=1,10)
      PRINT(6,914)
914   FCRPAT(/20X20FMOTOR VARIABLES ARE:)
      IF(PTYP.EQ.0)32,33
32    CCNTINUE
      PRINT(6,915)
915   FCRPAT(35X17HPCITOR TYPE= SHUNT)
      GO TO 34
33    PRINT(6,916)
916   FORMAT(35X1EHPCITOR TYPE= SERIES)
100 34  PRINT(6,917)PFATM,BSPD,AMAX
917   FCRPAT(35X12HFATED POWER-,F5.1,3H KW,/35X11HBASE SPEED-,F5.0,4H RP
      CM,/35X21HMAX ARMATURE CURRENT-,F5.0,5H AMPS)
40    CCNTINUE
      C
110 C   ENTER CONTROLLER VARIABLES. ENTER TYPE<CTYP> ON FIRST CARD: 1 IF
      C   FINITE STEP SWITCHING, 2 IF CHOPPER.
      C
      REAC*,CTYP
      IF(CTYP.EQ.1)141,50

```

```

115 41  CONTINUE
C
C   ENTER FINITE STEP CONTROLLER VARIABLES. FIRST CARD- NUMBER OF VOLT
C   ACE STEPS(1)CSTP). NEXT CARD- FRACTION OF FULL VOLTAGE FOR EACH
C   STEP(1)CSTP), AND EFFECTIVE SOURCE RESISTANCE(RBAT) FOR EACH STEP.
120 C
    READ*,ICSTP
    READ*,ICSTP(1),I=1,ICSTP,(RBAT(I),I=1,ICSTP)
    PRINT(6,920)(CSTP,CSTP(1),RBAT(1))
    DO 42 I=2,ICSTP
125 42  PRINT(6,921)CSTP(1),RBAT(1)
    920  FCRMAT(20X12,21H STEP CONTROLLER VARIABLES ARE:, /35X17HVOLTAGE FR
          EACTION=.F5.3,?17HSOURCE IMPEDANCE=.F6.4,5H OHMS)
    921  FCRMAT(52XF9.3,20XF5.3)
    GO TO 60
130 50  CONTINUE
C
C   ENTER CHOPPER CONTROLLER SOURCE IMPEDANCE(RBAT). MODEL ASSUMES 1.5
C   VOLTS JUNCTION LOSS AND 3X RESISTIVE LOSS.
C
135  READ*,RBAT(1)
    PRINT(6,929)RBAT(1)
    929  FCRMAT(20X33)CHOPPER CONTROLLER VARIABLES ARE:, /35X17HSOURCE IMPE
          DANCE=.F5.3,5H CHMS,/35X,32H ASSUMED JUNCTION DROP= 1.5 VOLTS,/35X2
          CRASSUMED RESISTIVE LOSSES= 32
140 C
    60  DC E1 I=1,ICSTP
    E1  RBAT(I)=RBAT(1)
C
C   ENTER BATTERY VARIABLES. FIRST CARD- NOMINAL TOTAL VOLTAGE(VNOM)
145 C   AND TOTAL MASS(BM).
C
    READ*,VNOM,BM
    BM=BM
    PRINT(6,926)VACM,BM
150 926  FCRMAT(20X22)BATTERY VARIABLES ARE:, /35X,16HNOMINAL VOLTAGE=.F4.0
      C,/35X13H BATTERFY MASS=.F5.01
C
C   ENTER HYBRID VARIABLES. FIRST CARD- 1 IF HYBRID,0 IF NOT. NEXT CARD
C   (IF IHYB=1)- HYBRID SPEED RATIO(HR), COUPLING EFFICIENCY(ETAH),
155 C   ENGAGEMENT SPEED(VH), AND NORMAL OPERATING TRANSMISSION GEAR(G)
C
    READ*,IHYB
    HR=0.
    VM=10C.
160  IF(IHYB.EQ.0)GO TO 71
    READ*,HR,ETAH,VH,ISH
    HR=10.
    PRINT(6,927)HR,ETAH,VM,ISH
165  927  FCRMAT(20X,32)HYBRID/MOTOR
          CR SPEED RATIO=.F6.3,/35X2CH COUPLING EFFICIENCY=.F5.1,1HZ,/35X17HEN
          CGAGEMENT SPEED=.F5.1,5HKM/HR,/35X22H TRANSMISSION POSITION=.I2,5H G
          CLEAR
    70  IS=ISH
    71  CONTINUE
170 C
    C   PROGRAM IS NOW READING INPUTTED DRIVING CYCLE SPEED SCHEDULE DATA.

```

```

C FIRST CARD- TIME INCREMENT(T), NUMBER OF DATA POINTS(NDATA). FOLLOWING CARDS- SPEED SCHEDULE(VX) IN MPH. LAST CARD- CONVERSION FACTOR(CO IF VX IN MPH, 1 IF VX IN KPH)(CCNV).
75 C
    READ*,T,NDATA
    NDATA=NDATA/18+1
    DO 80 J=1,NDATA
180   80 READ(15,901)(VX)(18*(J-1)+K),K=2,19
        READ*,CCNV
        IF(CCNV.EQ.C.181,82
        81  OC 81C1 J=1,NDATA
        81C1 VX(J+1)=VX(J+1)*1.602
        82  NDATA=NDATA/EO+1
185 C
    C ENTER PROGRAM OPTION. FIRST CARD- 0 IF SYSTEM EVALUATION, 1 IF SYSTEM DESIGN. NEXT CARD(IF IPROC=1)- MAXIMUM ALLOWABLE BATTERY DISCHARGE(OSMAX), AND MAXIMUM ALLOWABLE SPEED SCHEDULE DEVIATION (OVMAX).
190 C-
    READ*,IPROC
    IF(IPROC.EQ.C18201,8202
    82C1 PRINT(6,9301)
    93C FORPAT(1/20X33) SYSTEM EVALUATION OPTION SELECTED)
195   CC TO 8203
    8202 READ*,OSMAX,OVMAX
        PRINT(6,931)OSMAX,OVMAX
    931 FORPAT(1/2CX35) SYSTEM DESIGN OPTION SELECTED WITH:/35X22H MAX BATTER
        CY DISCHARGE-,F5.1,2H Z,/35X2CH MAX SPEED DEVIATION-,F5.1,6H KM/HR)
200  8203 DEV=0.
        OIS=0.
    83  VVI=0.
        V(1)=C.
        VX(1)=0.
205   W=0.
        WB=C.
        WH=0.
        D=0.
        KK=1
    210  PPAX=PRATM(PPBX
        MM=5.7599ALCGIC(PRATM)*21.5*HM
        H=(PP+BM+FM)/.74+.85*PM
        AMT=0.
        IF(C15.EQ.0.18302,8301
215  8301 FA=(P/P1)*.5*FA
        83C2 MI=P   S CIS=0.
        DO 160 II=1,NDATA
        PRINT(6,924)
    924 FORPAT(1H1,13CH TIME VELO-SCH VELO-ACT DEVIATION F-ROLL F-AIR
220   C F-ACCEL INPLT-POWER GEAR SHAFT-RPM CONTROLLER MTR ARM
        CBAT DISCHARGE)
        PRINT0," (SEC) (KM/HR) (KM/HR) (INT) (INT) (NT)
        C) (PTR) (HYB) SELECT (MTR)(HYB) STEP/FIELD VOLTS AMPS E
        C)#
        PRINT0," "
        OC 16C III=1,EC
        I=III+III*60-59
        IF(VX(II).GE.99.9)170,85

```

```

25   VBAT=(73.1+.02E9*D15-.0C1C1*D15+01S1*VN04/72.
23C  V(I)=VX(I)
      KKK=0
      90  VV=V(I)*.2778
          DELTAV=.02
          A=0.
235  VLT=0.
      MS=0.
      MSH=0.
      MPP=0
      PRCH=0.
240  PAVL=0.
      MCF=1.02
      VVA=(VV1+VV2)/2.
      IF(1S.EC.0)192,91
245  91  CALL PTRSP0(VVA,RR,AR,GR,UPSHFT,DNSHFT,IS,KK,MS)
      MCF=MCF*.C0C294*(AR*GR(KK))/RR)**2.
      92  FR=(CR*.CCCCOC2C9*VVA**2.81)*9.81
          FAIR=VVA**2.*176.4*FA*CD/(273.*TMP)
          FACC=P*(VV-VV1)/T*MCF
          F=FR+FAIR+FACC
          P=F*VVA/1000.
          IF(VVA.EC.0.)CC TO 153
9002  PSPD=V(I)/VMAX*100.
      PP=P/PMAX*1C0.
      IF(PP.EC.0.)192C2,9201
250  92C1  ETAA=55.8-(.01217*PSPD*PSPD+.8879*PSPD*4.261)/ABS(PP)
      92C2  IF(1S.EC.0)192C3,9204
      92C3  MS=ESPD
          CALL TRASEFF(P,ETAA,PRATT,VVA,RR,AR,BSPD,TSTP,ITSTP,ETAT,ETAI)
          GO TO 1C0
      .26C  9204  IF(PP.EC.0.)193,9205
      92C5  PSPET=PSPD*(CR(KK))/CR(1S)
          IF(CR(KK).LT.1.193,94
          93  EMAX=EXP(.03*(I,-1./CR(KK)))
          GO TO 95
      265  94  EPAX=EXP(.03*(I,-1./CR(KK)))
      95  ETA=EPAX*(99.-1.004C05*PSPD*PSPD+.1849*PSPD*1.565)/ABS(PP))
      100  IF(PP.GT.0.)1C1,102
      101  PRCD=P*ETAA/ETA*10000.
          GO TO (11C,11C1,1101)CTYP
      27C  102  PAVL=P*ETAA/ETA/10000.
          GO TO 151
      110  CALL VSTEP(PRC0,MS,RARM,KMOT,VBAT,1CSTP,CSTP,A,PAVL,AMAX,PRATH,
          CMSTP,14STP,ETAP,MPP,REAT,VLT,1HYB,MR,ETAH,PRCH,V(I),VM,MTYP,RFLO)
          GO TO 111
      275  1101 CALL VCHCP(PTYP,RARM,RFLO,KPOT,AMAX,PRATH,14STP,MSTP,ETAM,RBAT,VBA
          CT,1HYB,MR,ETAH,VM,PRCD,MS,V(I),A,VLT,PAVL,PRCDH)
      111  IF(ABS((PAVL-PRCD)/V(I)).GT..0001)DELTAV=.5
      112  IF(KKK.EC.2)121,118
      118  TF(PAVL.GT.PRC0)119,120
      28C  119  V(I)=V(I)+DELTAV
          KKK=1
          GO TO 90
      120  IF(KKK.EC.1)152,121
      121  IF(PAVL.LT.PRC0)122,152
      285  122  V(I)=V(I)-DELTAV

```

```

      KKK=2
      GO TO 90
151  W=6E+T/3600.*PAVL
      GO TO 153
250  152  W=B+T/3600.*PAVL
              W=B+T/3600.*PRODH
      153  IT=IT-T
              VV1=VV
              PRCCF=PAVL-PRCCH
295      IF(V(1).GE.VH.AND.IHYB.EQ.1)MSH=MS*HR
              D=D+VVA*T/1000.
              DEV=V(1)-VX(1)
              PRINT(6,918)IT,VX(1),V(1),DEV,FR,FAIR,FACC,PRODE,PRCOH,KK,MS,RSH,R
              CMP,FLC,VLT,A,CIS
300  918  FCR=AT(1X14,F9.1,2F10.1,F10.0,2F8.0,F7.1,F6.1,I5,F8.0,F6.0,I4,F7.0
              C,F7.1,F6.0,F12.4)
              IF(***.EQ.0)MPP=1
      155  CALL RATOIS(TPP,A,AHT,T,IT,CIS,CSTP(MMM),VNOM,BM)
              IF(IPRCC.EC.0)GO TO 160
      305  IF(CIS.GT.OSMAX)1551,1553
      1551  BM=BP+100.
              DO 1552 LL=1,ICSTP
      1552  RAAT(LL)=RAAT1(LL)*BM/8M
              PRINT(6,92818P)
310      PRINT0," TOTAL TIME= ",IT," SECS"
      928  FORPAT(1/20X92F00000) CYCLE TERMINATED DUE TO INSUFFICIENT BATTERY C
              CAPACITY TO MEET RANGE REQUIREMENTS *****,/35X24HNEXT ITERATION WILL
              CL USE:/40X14H BATTERY MASS= ,F5.0)
              GO TO 83
315  1553  IF(CFV.LT.0.0MAX)156,160
      156  PRAT=PRATH+1.
              R=PRAT/(PRATP-1.)
              BP=BM*R**.5
              DO 157  L=1,I(STP
320  157  RAAT(L)=RAAT1(L)*BM/8M
              RFLC=RFLD/R
              RARP=R3R*/R
              KFCI=KFCI/R
              AFAY=AFAY*OR
      325  PRINT(6,9251PRATH,BM
              PRINT0," TOTAL TIME= ",IT," SECS"
      925  FCR=AT(25)81H40000 CYCLE TERMINATED DUE TO INSUFFICIENT POWER TO MEET
              POWER REQUIREMENTS *****,/35X24HNEXT ITERATION WILL USE:/40X13
              CH=0.0PCER= ,F4.1/40X14H BATTERY MASS= ,F5.0)
      330  GO TO 83
      160  CONTINUE
      170  PRINT0," TOTAL CYCLE TIME (MIN) ="
              TIME=T*(IT-1)/60.
              PRINT(6,919)TIME
      335  919  FCR=AT(F10.4)
              PRINT0," TOTAL CYCLE DISTANCE (KM) ="
              PRINT(6,919)D
              WF=W-WH
              PRINT0," TOTAL MOTOR INPUT ENERGY (KW-HR) ="
              PRINT(6,919)MP
              PRINT0," TOTAL ENGINE INPUT ENERGY (KW-HR) ="
              PRINT(6,919)HM

```

```

PRINT," TOTAL REGENERATION ENERGY AVAILABLE (KW-HR) --"
PRINT(6,919)HE
345 PRINT," BATTERY DISCHARGE AT END OF CYCLE (%) --"
PRINT(6,919)DIS
GAS=LHO*.56*FC*EST/0
ELECT=WH*EC*COST/.6/D
PRINT," AVG CYCLE ELECTRICAL COST ($/KMH) --"
PRINT(6,919)ELECT
PRINT," AVG FETROLEUM FUEL COST ($/KMH) --"
PRINT(6,919)GAS
IF(IPROG.EQ.01)GO TO 172
PRINT," FINAL VEHICLE PARAMETERS ARE:--"
PRINT,"      MOTOR POWER= ",PRATH," BATTERY MASS= ",BM
PRINT,"      TOTAL MASS= ",M," FRONTAL AREA= ",FA
172 END

```

```

1 SUBROUTINE PTRSPO(VVA,RR,AR,GR,UPSHFT,DNSHFT,IS,K,RMS)
C DIMENSION GR(1C)
C
5 C THIS SUBROUTINE COMPUTES MOTOR SPEED FOR MULTI-SPEED TRANSMISSIONS
C AND DRIVING CYCLE REQUIREMENTS.
C
100 RPS=VVA*99.549/RR*AR*GR(K)
101 IF (RPS.GT.UPSHFT)101,103
102 IF(K.LT.IS)102,106
103 K=K+1
104 IF (RPS.LT.DNSHFT)104,106
105 K=K-1
106 CC TO 100
107 RETURN
END

```

```

1      SUBROUTINE VCHCP1(TYP,RAM=,RFLD,RKHT,AMAX,PRATH,INSTP,RNSTP,ETAM,
C      CRAT,VRAT,IHY2,HR,ETAH,VH,P,P=S,V,A,VLT,PAVL,PRCDH)
C      DIMENSION RNSTP(110),ETA=(10,30)

2      C
3      C THIS SUBROUTINE CALCULATES MOTOR POWER DEVELOPED AND CURRENT
4      C REQUIRED FOR SCR CHOPPER VOLTAGE CONTROLLERS WITH DC MOTORS. IT
5      C ASSUMES 1.5 VOLTS JUNCTION LOSS AND 3% COPPER LOSS.
6      C

7      KK=0
8      C=RPS/RKHOT
9      PRCC=P*ICCG.
10     CALL PTREFF(PRCD,PRATH,RMS,RNSTP,INSTP,ETAM,ETA)
11     IF(PTYP.EC.C14C1,402
12     401 EAIA=PRCD/ETA*100.*C/(RFLD+RARM*RFLD/(RFLD-C))
13     IF(EAIA.LT.PRCC)EAIA=PRCD
14     VLT=(EAIA*RARM*RFLD*RFLC/C/(RFLD-C))*0.5
15     VPAX=AMAX*(RARM*RFLD/(RFLD-C))
16     A=EAIA*RFLD/VLT*C
17     GO TO 403
18     402 RTOT=RARM*RFLC
19     EAIA=PRCC*C/ETA/(C+RTOT)
20     IF(EAIA.LT.PRCC)EAIA=PRCD
21     A=(EAIA/C)*0.5
22     VMAX=AMAX*(RBAT*1.03*(RTOT+C))+1.5
23     VLT=A*VMAX/AMAX
24     403 IF(VLT.GT.VPAX)KK=1 SVLT=VPAX SA=AMAX
25     IF(VLT.LE.VPAX)404,406
26     404 IF(KK.EQ.0)405,407
27     405 PAVL=P
28     RETURN
29     406 VLT=VBAT
30     407 IF(PTYP.EQ.C14C8,409
31     408 EAIA=C*VLT*VLT/RARM/RFLD*(1.-C/RFLD)
32     A=EAIA/C/VLT*RFLD
33     GO TO 410
34     409 EAIA=(VLT-1.5)/(RBAT*1.03*(RTOT+C))*2.0C
35     A=(EAIA/C)*0.5
36     CALL PTREFF(EAIA,PRATH,RMS,RNSTP,INSTP,ETAM,ETA)
37     IF(PTYP.EC.C14C1,412
38     411 PAVL=ETA*(EAIA+A*A*RARM*VLT*VLT/RFLD)*100000.
39     412 PAVL=ETA*(EAIA+A*A*RTOT)/100000.
40     GO TO 413
41     413 IF(PAVL.GT.EAIA/1000.)PAVL=EAIA/1000.
42     IF(IHYB.EC.1.AND.V.GE.VH)414,417
43     414 PAVLM=1.000E7*FMS*HR+.991*ETAH/100.
44     PRCDH=P-PAVL
45     IF(PAVLM.GE.PRCDH)415,416
46     415 PAVL=P
47     RETURN
48     416 PAVL=PAVLH+PAVL
49     PRCDH=PAVLH
50     417 RETURN
51     END

```

```

1      SUBROUTINE VSTEP1P,RMS,RARM,RKNOT,VRAT,ICSTP,CSTP,A,PAVL,AMAX,PRAT
2      CM,RSTP,INSTP,ETAM,M,RBAT,VLT,IHY4,HR,ETAM,PRCOH,V,VH,MTYP,RFLD)
3      DIMENSION CSTP(5),RSTP(1C),ETAM(10,30),RBAT(5)

4      C
5      C      THIS SUBROUTINE CALCULATES MOTOR POWER DEVELOPED AND CURRENT
6      C      REQUIRED FOR FINITE STEP VOLTAGE CONTROLLERS WITH DC MOTORS.
7      C

8      MM=0
9      IF(MTYP.EQ.0.AND.RMS.LT.1000.)RMS=1000.

10     501  M=M+1
11      C=RMS/RKNOT
12      DV=A*RBAT(M)
13      5011 VLT=CSTP(4)*VEAT-DV
14      IF(MTYP.EQ.0)5111,5112
15      5111 EAIA=C*VLT+VLT/RARM/RFLD*(1.-C/RFLD)
16      A=EAIA*RFLD/VLT/C
17      GO TO 5113
18      5112 RTOT=RFLD*RARM
19      EAIA=(VLT-YLT+C/(RTOT+C))/RTOT)**2.*C
20      A=(EAIA/C)**.5
21      5113 DV2=A*RBAT(M)
22      IF(A>5(DV2-CV).GT.0.3)5012,5013
23      5012 DV=DV2
24      GO TO 5C11
25      5013 CALL PTEFF(EAIA,PRATH,RMS,RSTP,INSTP,ETAM,ETAB)
26      IF(MTYP.EC.C)>211,5212
27      5211 PAVL=ETA*(EAIA+A*A*RARM+VLT*VLT/RFLD)/100000.
28      GO TO 5213
29      5212 PAVL=ETA*(EAIA+A**2.*RTCT)/100000.
30      5213 IF(PAVL.GT.EAIA/1000.)PAVL=EAIA/1000.
31      5015 IF(P.EQ.015C2,507
32      502  IF(P.GT.1.AND.P.GT.1M4X15C6,504
33      504  IF(PAVL.GE.(P+.81)5061,505
34      505  IF(.LT.ICSTP15C61,5061
35      5061 IF(PAVL.LT.P+.4AD.(HYB.EC.1.AND.V.GE.VH.AND.M.EQ.ICSTP15C64,507
36      5C64 PAVLM=1.000E7*FMS*HR+.991*ETAH/100.
37      PRCDH=P-PAVL
38      IF(PAVLM.GE.PRCDH)5C62,5063
39      5C62 PAVL=P
40      RETURN
41      5063 PAVL=PAVL+PAVLH
42      PRCDH=PAVLH
43      RETURN
44      506  M=M-2
45      MM=1
46      GO TO 501
47      507  RETURN
48      END

```

```

1      SUBROUTINE PTREFF(ETA1A,PRATH,RMS,RMSTP,IMSTP,ETAM,ETA)
2      DIMENSION ETAP(10,30),RMSTP(10)
3
4      C
5      C      THIS SUBROUTINE PERFORMS A POLINEAR INTERPOLATION FOR MOTOR
6      C      EFFICIENCY(ETA) AS INPUTTED FOR DISCRETE VALUES OF MOTOR SPEED
7      C      (RMSTP) AND PERCENT OF RATED POWER(PP).
8
9      C      PP=ETA1A/PRATH/10.
10     K=1
11     KK=1
12     600 IF(RPS.LE.RPSTP(K))603,601
13     601 IF(K.LT.IMSTP)602,603
14     602 K=K+1
15     GO TO 600
16     603 IF(PP.LE.(KK+1))605,6031
17     6031 IF(KK.LT.30)604,605
18     604 KK=KK+1
19     GO TO 603
20     605 IF(K.EQ.1)606,607
21     606 IF(KK.EQ.1)608,609
22     607 CC=(RPS-RPSTP(K-1))/(RMSTP(K)-RMSTP(K-1))
23     ETA2=(ETAM(K,KK)-ETAM(K-1,KK))*CC+ETAM(K-1,KK)
24     IF(KK.EQ.1)611
25     608 ETA=ETAM(1,1)
26     RETURN
27     609 ETA1=ETAM(K,KK-1)
28     ETA2=ETAM(K,KK)
29     GO TO 612
30     610 ETA=ETA2
31     RETURN
32     611 ETA1=(ETAM(K,KK-1)-ETAM(K-1,KK-1))*CC+ETAM(K-1,KK-1)
33     612 ETA=(ETA2-ETA1)*(PP-(KK-1)*10.)/10.+ETA1
34     RETURN
35     END

```

```

1      SUBROUTINE TRSEFF(P,ETAA,PRATT,VVA,RR,AR,BSPD,TSTP,ITSTP,ETAT,ETA
C
C      DIMENSION TSTP(10),ETAT(10,20)
C
C      THIS SUBROUTINE PERFORMS A BILINEAR INTERPOLATION FOR CVT EFFICI-
C      ETAT) AS INPUTTED FOR DISCRETE VALUES OF SPEED RATIOS(TSTP)
C      AND PERCENT RATED POWER(PP).
C
C      PP=P*ETAA/PRATT
10     OSS=9.549*VVA/RR*AR
      SP=CSS/BSPD
      K=1
      KK=1
      700 IF(SR.LE.TSTP(K))703,701
15     701 IF(K.LT.ITSTP)702,703
      702 K=K+1
      CC TO 700
      703 IF(PP.LE.(KK*5.))705,703L
      703L IF(KK.LT.20)704,705
20     704 KK=KK+1
      CC TO 703
      705 IF(K.EQ.1)706,707
      706 IF(KK.EQ.1)708,709
      707 CC=(SR-TSTP(K-1))/(TSTP(K)-TSTP(K-1))
25     ETA2=(ETAT(K,KK)-ETAT(K-1,KK))*CC+ETAT(K-1,KK)
      IF(KK.EQ.1)71C,711
      708 ETA=ETAT(1,1)
      RETURN
      709 ETA1=ETAT(K,KK-1)
      ETA2=ETAT(K,KK)
      CC TO 712
      710 ETA=ETA2
      RETURN
      711 ETA1=(ETAT(K,KK-1)-ETAT(K-1,KK-1))*CC+ETAT(K-1,KK-1)
35     712 ETA=(ETA2-ETA1)*(PP-(KK-1)*5.1/5.+ETA1
      RETLRN
      ENO

```

```

1      SUBROUTINE BATCIS(TMP,A,AHT,T,IT,DIS,CSTP,VNDF,BM)
C
C      THIS SUBROUTINE COMPUTES TOTAL BATTERY DISCHARGE<Z>(DIS) FOR LEAD
C      ACID BATTERIES OF GOLF-CART TYPE CONSTRUCTION. IT IS TEMPERATURE
C      CORRECTED AND USES A MODIFIED FRACTIONAL-UTILIZATION METHOD WITH
C      CORRECTIONS FOR CHANGING CURRENTS AND RECLUPERATION PERIODS.
C
C      A=A*CSTP*35C./2*VNDF/72.
10     APT=AHT*A*T/36C0.
      AH=(195.-.633*A+.000913*A*A)*(1.014*TMP+.65)
      AVG=AHT/IT*36C0.
      APA=(195.-.633*AVG+.000913*AAVG*AAVG)*(1.014*TMP+.65)
      IF(A.EQ.0.)E01,802
      E01 RA=0.
      GO TO 805
      802 IF(A.GT.AAVG)E03,804
      803 RA=AAVG/A
      CC TO 805
      804 RA=A/AAVG
20     805 DIS=(AHT/AH*RA+AHT/AHA*(1.-RA))/100.
      RETURN
      ENO

```

UNCLASSIFIED

SECURITY CLASSIFICATION OF THIS PAGE

REPORT DOCUMENTATION PAGE

1a. REPORT SECURITY CLASSIFICATION UNCLASSIFIED		1b. RESTRICTIVE MARKINGS	
2a. SECURITY CLASSIFICATION AUTHORITY N/A		3. DISTRIBUTION/AVAILABILITY OF REPORT Approved for public release - distribution unlimited	
2b. DECLASSIFICATION / DOWNGRADING SCHEDULE N/A			
4. PERFORMING ORGANIZATION REPORT NUMBER(S) AU-AFIT-EN-TR-83-4		5. MONITORING ORGANIZATION REPORT NUMBER(S)	
6a. NAME OF PERFORMING ORGANIZATION School of Engineering	6b. OFFICE SYMBOL (if applicable) AFIT/ENY	7a. NAME OF MONITORING ORGANIZATION	
6c. ADDRESS (City, State and ZIP Code) Air Force Institute of Technology Wright-Patterson AFB, OH 45433		7b. ADDRESS (City, State and ZIP Code)	
8a. NAME OF FUNDING/SPONSORING ORGANIZATION	8b. OFFICE SYMBOL (if applicable)	9. PROCUREMENT INSTRUMENT IDENTIFICATION NUMBER	
8c. ADDRESS (City, State and ZIP Code)		10. SOURCE OF FUNDING NOS.	
		PROGRAM ELEMENT NO.	PROJECT NO.
		TASK NO.	WORK UNIT NO.
11. TITLE (Include Security Classification) Electric Vehicle Modelling and Simulation			
12. PERSONAL AUTHOR(S) Aaron R. DeWispelare			
13a. TYPE OF REPORT	13b. TIME COVERED FROM _____ TO _____	14. DATE OF REPORT (Yr., Mo., Day) August 1983	15. PAGE COUNT 70
16. SUPPLEMENTARY NOTATION			
17. COSATI CODES		18. SUBJECT TERMS (Continue on reverse if necessary and identify by block number) Electric Automobiles, Electric Propulsion, Electric Motor Control Theory, Computerized Simulation	
19. ABSTRACT (Continue on reverse if necessary and identify by block number) The forecasting of the performance of electric vehicles has revealed many discrepancies when compared to actual test data. An electric vehicle computer simulation program was developed to ameliorate this deficiency. The approach was to establish a very comprehensive and flexible vehicle model and simulate its operation on a realistic driving cycle. The driving cycle selected was the Federal Urban Driving Sequence. A thorough vehicle model was established that incorporates aerodynamic drag, rolling resistance, both rotational and translational inertial effects, and component by component dynamic power train efficiencies. Battery discharge performance is tracked by a fractional-utilization algorithm with corrections for short-term discharge effects. The simulation compares required power obtained from the driving cycle speed schedule and vehicle model characteristics with the available power at the motor for each time increment of the driving cycle to compute battery fraction used and deviation from the speed schedule when available power is insufficient. These results of the simulation can be used to evaluate an existing vehicle's performance or, if			
20. DISTRIBUTION/AVAILABILITY OF ABSTRACT <input type="checkbox"/> UNCLASSIFIED/UNLIMITED <input type="checkbox"/> SAME AS RPT. <input type="checkbox"/> OTIC USERS <input type="checkbox"/>		21. ABSTRACT SECURITY CLASSIFICATION	
22a. NAME OF RESPONSIBLE INDIVIDUAL PETER J. TORVIK		22b. TELEPHONE NUMBER (Include Area Code) (513) 255-3069	22c. OFFICE SYMBOL AFIT/ENY

UNCLASSIFIED

SECURITY / CLASSIFICATION OF THIS PAGE

Item 19. (cont'd)

desired, to develop vehicle parameters to obtain a specified performance level. An application of the program to develop a suburban passenger vehicle is included to demonstrate the simulation's utility. A test bed vehicle was constructed and tested to verify the simulation. Additional aspects such as microprocessor based controllers including implementation of an optimal control law were investigated to gain insight into the efficiency and performance trade-offs of such a system.

END

FILMED

5-84

DATIRE